UNIVERSITY OF HELSINKI REPORT SERIES IN PHYSICS

HU-P-D180

Irradiation effects in graphene and related materials

Ossi Lehtinen

Division of Materials Physics
Department of Physics
Faculty of Science
University of Helsinki
Helsinki, Finland

ACADEMIC DISSERTATION

To be presented, with the permission of the Faculty of Science of the University of Helsinki, for public criticism at the auditorium E204 of the Department of Physical Sciences (Physicum), on May the 30th, 2011, at 12 o'clock p.m.

HELSINKI 2011

ISBN 978-952-10-6877-5 (printed version)
ISSN 0356-0961
Helsinki 2011
Helsinki University Printing House (Yliopistopaino)

ISBN 978-952-10-6878-2 (PDF version)
http://ethesis.helsinki.fi/
Helsinki 2011
Electronic Publications @ University of Helsinki (Helsingin yliopiston verkkojulkaisut)

Ossi Lehtinen **Irradiation effects in graphene and related materials**, University of Helsinki, 2011, 67 p.+appendices, University of Helsinki Report Series in Physics, HU-P-D180, ISSN 0356-0961, ISBN 978-952-10-6877-5 (printed version), ISBN 978-952-10-6878-2 (PDF version)

Classification (PACS): 61.48.De, 61.48.Gh, 61.80.Az, 61.80.Jh, 68.37.Og, 78.30.-j, 61.72.Cc
Keywords: graphene, white graphene, carbon nanotubes, boron nitride nanotubes, radiation effects, simulation, ion irradiation, transmission electron microscopy, raman spectroscopy.

ABSTRACT

Nanomaterials with a hexagonally ordered atomic structure, *e.g.*, graphene, carbon and boron nitride nanotubes, and white graphene (a monolayer of hexagonal boron nitride) possess many impressive properties. For example, the mechanical stiffness and strength of these materials are unprecedented. Also, the extraordinary electronic properties of graphene and carbon nanotubes suggest that these materials may serve as building blocks of next generation electronics. However, the properties of pristine materials are not always what is needed in applications, but careful manipulation of their atomic structure, *e.g.*, via particle irradiation can be used to tailor the properties. On the other hand, inadvertently introduced defects can deteriorate the useful properties of these materials in radiation hostile environments, such as outer space.

In this thesis, defect production via energetic particle bombardment in the aforementioned materials is investigated. The effects of ion irradiation on multi-walled carbon and boron nitride nanotubes are studied experimentally by first conducting controlled irradiation treatments of the samples using an ion accelerator and subsequently characterizing the induced changes by transmission electron microscopy and Raman spectroscopy. The usefulness of the characterization methods is critically evaluated and a damage grading scale is proposed, based on transmission electron microscopy images. Theoretical predictions are made on defect production in graphene and white graphene under particle bombardment. A stochastic model based on first-principles molecular dynamics simulations is used together with electron irradiation experiments for understanding the formation of peculiar triangular defect structures in white graphene. An extensive set of classical molecular dynamics simulations is conducted, in order to study defect production under ion irradiation in graphene and white graphene.

In the experimental studies the response of carbon and boron nitride multi-walled nanotubes to irradiation with a wide range of ion types, energies and fluences is explored. The stabilities of these structures under ion irradiation are investigated, as well as the issue of how the mechanism of energy transfer affects the irradiation-induced damage. An irradiation fluence of 5.5×10^{15} ions/cm^2 with 40 keV Ar^+ ions is established to be sufficient to amorphize a multi-walled nanotube. In the case of 350 keV He^+ ion irradiation, where most of the energy

transfer happens through inelastic collisions between the ion and the target electrons, an irradiation fluence of 1.4×10^{17} ions/cm^2 heavily damages carbon nanotubes, whereas a larger irradiation fluence of 1.2×10^{18} ions/cm^2 leaves a boron nitride nanotube in much better condition, indicating that carbon nanotubes might be more susceptible to damage via electronic excitations than their boron nitride counterparts. An elevated temperature was discovered to considerably reduce the accumulated damage created by energetic ions in both carbon and boron nitride nanotubes, attributed to enhanced defect mobility and efficient recombination at high temperatures. Additionally, cobalt nanorods encapsulated inside multi-walled carbon nanotubes were observed to transform into spherical nanoparticles after ion irradiation at an elevated temperature, which can be explained by the inverse Ostwald ripening effect.

The simulation studies on ion irradiation of the hexagonal monolayers yielded quantitative estimates on types and abundances of defects produced within a large range of irradiation parameters. He, Ne, Ar, Kr, Xe, and Ga ions were considered in the simulations with kinetic energies ranging from 35 eV to 10 MeV, and the role of the angle of incidence of the ions was studied in detail. A stochastic model was developed for utilizing the large amount of data produced by the molecular dynamics simulations. It was discovered that a high degree of selectivity over the types and abundances of defects can be achieved by carefully selecting the irradiation parameters, which can be of great use when precise pattering of graphene or white graphene using focused ion beams is planned.

Contents

1 Introduction

The history of human kind can be written in large parts in terms of what materials we have been able to harness for our benefit. This is evident already from the nomenclature of the prehistoric ages, where the time periods are named after the most advanced materials in use (*e.g.* the Bronze Age). Although such strict division cannot be assigned in the modern times, the impacts of new materials on human potential are undeniable. Indeed, the world would have been quite a different place without discoveries such as semi-conductors and plastics, or earlier ones like concrete, glass, and steels, among many others.

Such history defining steps in technology have by no means reached the end of the line. Instead, they have become so frequent that discrete steps are impossible to distinguish. Today, this is highlighted by the advent of nanomaterials in general and the newly found nanoscale allotropes of carbon, such as graphene [1] and carbon nanotubes [2–4] with their boron-nitride counterparts [5–7] as specific examples. Many of the properties of these materials are unique and absent in any of the preceding materials. As an example, the tensile strength of carbon nanotubes is approximately one hundred times higher than that of steel: where a 5 mm thick steel wire is needed to lift a 2000 kg car, in theory a 0.5 mm thick nanotube bundle can handle the same load[1]. Such leaps in material properties open up possibilities earlier unimaginable: Even building an elevator to space moving along a rope made from carbon nanotubes has been seriously considered, *e.g.*, by NASA [9].

No technology is born ready, however, and the route to full utilization of the potential of these materials remains uncharted. The amazing tensile strength of individual nanotubes, for example, is not readily translated to macroscopic ropes of nanotubes, as the individual tubes slip easily relative to each other [10], and atomic scale defects, which are always present in some quantities in real materials, can lower their strength considerably [11–14]. On the other hand, the individual tubes can form inter-tube covalent bonds at the defect sites, which can greatly enhance the mechanical properties of the ropes [10, 15].

Atomic-scale defects tend to influence many of the properties of any nanoscale material: Mobility of charge carriers in graphene is high, due to the unusual linear dispersion relation of conducting electrons [16], but defects can have a profound influence on the conduction properties. The resistivity of a graphene sheet can quickly rise due to defects in the lattice. A

[1] Assuming a tensile strength of 100 GPa for the nanotubes [8] and 1 GPa for steel (the exact value varies depending on the type of steel).

band-gap can be opened if the perfect structure is modified [17–21], which can be highly advantageous if electronic devices are to be built using graphene. Similarly, the electronic properties of hexagonal boron nitride structures can be affected by the presence of defects [22] and the electronic properties can be tailored in a controllable manner by modifying the structure [23,24].

Bombardment of materials with energetic particles, such as ions or electrons, has been used to introduce defects in nanoscale targets [10, 25–28]. At the present time, ion and electron beams can be focused to spots in the nanometer scale, and these beams can be used to carve desired patterns in the targets [18, 29, 30]. On the other hand, materials can be used in applications where the structures are exposed to particle radiation involuntary, such as in outer space, where inevitably some defects will be introduced.

Both in the case of intentional irradiation, as well as in the case of inadvertent radiation exposure, it is of great importance to understand the response of the materials. This matter is addressed in this thesis. In publications **I**, **II**, and **III** the response of multi-walled carbon and boron nitride nanotubes to ion irradiation is explored experimentally, by first exposing samples to ion irradiation using a particle accelerator, and later characterizing the induced changes via transmission electron microscopy and Raman spectroscopy. In publications **IV**-**VII** theoretical investigations on defect production in carbon (graphene) and boron nitride (white graphene) monolayers under ion and electron irradiation, based on multi-scale atomistic simulations, are reported on.

Based on the experimental and theoretical data reported in publications **I**-**VII**, insights into defect production mechanisms are gained. The peculiarities of the behavior of the atomically thin targets under irradiation are studied, and conclusions are drawn on how they can be harnessed in order to gain higher level of control over the atomic structure of the targets, *e.g.*, during patterning of graphene using focused ion beams. In this summary part of this thesis, special attention is paid to similarities and differences of the irradiation response of the carbon and boron nitride nanostructures.

2 Purpose and structure of this study

The purpose of this thesis is to study the response of four closely related nanosystems, *i.e.*, carbon nanotubes, boron nitride nanotubes, graphene, and white graphene, to particle irradiation. First, the thesis aims to experimentally map the resilience of nanotubes exposed to ion irradiation, and to asses how quickly they will degrade under such treatment. Second, theoretical predictions of the evolution of the monolayers under particle bombardment are made, which can be used to gain control over the types and abundances of defects produced, *e.g.*, when patterning graphene using focused ion beams.

This thesis consists of this summary and seven articles which have been published (6) or submitted (1) for publication in international peer-reviewed journals. The articles are referred to by bold face Roman numerals in this summary, and they are included at the end of this thesis.

The summary consists of eight sections, including the introduction and this description of the thesis. In section three, the studied materials are introduced, starting from the bonding characteristics of the materials, going through their structure and most important properties, and ending up on a review of the effects of atomic scale defects on the properties of the studied materials. In section four, the employed experimental methods are reviewed. The used theoretical methods are introduced in section five. Section six concentrates on the experimental results presented in publications **I-III** and section seven focuses on the theoretical work presented in publications **IV-VII**. Finally, the findings are summarized in section eight.

2.1 Summaries of the original publications

Publication I: Ion irradiation of carbon nanotubes encapsulating cobalt crystals, O. Lehtinen, L. Sun, T. Nikitin, A. Krasheninnikov, L. Khriachtchev, J. Rodriguez-Manzo, M. Terrones, F. Banhart,and J. Keinonen, *Physica E* **40**, 2618 (2008)

In this publication the response of multi-walled carbon nanotubes encapsulating cobalt nanorods to ion irradiation was studied. The samples were irradiated at elevated temperatures ($500 - 800$ K) with ions of various species (H, He, and C) and various energies ($40 - 380$ keV). The samples were investigated using transmission electron microscopy and Raman spectroscopy. The main observations in the publication were that the elevated temperature did not protect the nanotube structure, contrary to the case of electron irradiation, that there was no pressure build up inside the the nanotubes, contrary to what had been observed under electron irradiation as evidenced by the contraction of the encapsulated cobalt

nanorods, but rather the cobalt rods were transformed into small spherical nanoparticles on and embedded in the nanotube walls.

Publication II: Ion irradiation of multi-walled boron nitride nanotubes,
O. Lehtinen, T. Nikitin, A. V. Krasheninnikov, L. Sun, L. Khriachtchev, F. Banhart, T. Terao, D. Golberg, and J. Keinonen, *Physica Status Solidi C* **7**, 1256 (2010).

This publication focused on the ion irradiation response of multi-walled boron nitride nanotubes. In this study, the samples were irradiated with 40 keV Ar^+ ions and 350 keV He^+ ions, with various fluences at room temperature as well as at elevated temperatures. Again the characterization methods were transmission electron microscopy and Raman spectroscopy. A fluence of 2×10^{15} ions/cm^2 of 40 keV Ar^+ ions was observed to be enough to almost completely amorphize a boron nitride nanotube, whereas a dose of 1.2×10^{18} ions/cm^2 of 350 keV He^+ left the sample in much better condition. An elevated temperature of $\sim$900 K was observed to protect the nanotubes from accumulation of damage, attributed to mobility of point defects at this temperature.

Publication III: Characterization of ion-irradiation-induced defects in multi-walled carbon nanotubes,
O. Lehtinen, T. Nikitin, A. V. Krasheninnikov, L. Sun, F. Banhart, L. Khriachtchev, and J. Keinonen, submitted for publication.

This publication put emphasis on the characterization methods employed in the previous two studies. A universal damage grade scale was constructed for assigning a numerical value to the condition of a multi-walled nanotube after an irradiation treatment based on transmission electron microscopy. Such a scale facilitates comparison of the effects of different treatments in an organized manner. Shortcomings of Raman spectroscopy in characterizing irradiation induced damage was studied, related to the typically non-isotropic distribution of damage induced by ion irradiation and Raman spectroscopy's inability to distinguish the differently affected areas. The specific effects of He, C, and Ar ion irradiation were studied. Amorphizing fluence of 5.5×10^{15} ions/cm^2 with 40 keV Ar^+ ions was determined. A more systematic study of high temperature annealing was conducted, and it was observed that an elevated temperature in fact does reduce accumulated damage under ion irradiation in carbon nanotubes, contrary to the observation in publication **I**. Additionally, it was observed, that the amount of damage produced by 350 keV He^+ ion irradiation was higher than what would be expected from taking only atomic collisions into account. This indicates that the quasi-one-dimensional carbon nanotubes could be more vulnerable to damage through electronic excitations than bulk graphite.

Publication IV: Effects of ion bombardment on a two-dimensional target: Atomistic simulations of graphene irradiation,
O. Lehtinen, J. Kotakoski, A. V. Krasheninnikov, A. Tolvanen, K. Nordlund, and J. Keinonen, *Physical Review B* **81**, 153401 (2010).

In this publication abundance and types of defects produced by impacts of He, Ne, Ar, Kr, and Xe ions on graphene were estimated. It was established that simple damage estimation methods based on binary collisions of the ions and target atoms do not accurately describe the induced damage, and for this reason analytical potential molecular dynamics simulations modelling the ion impacts were conducted. Observing that atomically thin graphene is almost transparent to high energy ions, and taking earlier reports on graphene's gas-holding capacity into account, graphene was proposed to be used as the ultimate membrane for external beam experiments, where the targets cannot be put in high vacuum required for the operation of ion beams.

Publication V: Electron knock-on damage in hexagonal boron nitride monolayers,
J. Kotakoski, C. H. Jin, O. Lehtinen, K. Suenaga, and A. V. Krasheninnikov, *Physical Review B* **82**, 113404 (2010).

This publication concentrated on modeling the response of white graphene to electron irradiation. Holes produced by electron irradiation had been observed to have a well defined triangular shape and further on, all the triangles had the same orientation. First-principles molecular dynamics simulations were used to obtain the displacement threshold energies (*i.e.* the minimum amount of kinetic energy required to eject a target atom) for boron and nitrogen atoms in white graphene. A kinetic Monte Carlo model was developed based on the obtained threshold energies. The threshold energies were observed to be highly asymmetric for boron and nitrogen and the experimentally observed shape of the holes was reproduced in the kinetic Monte Carlo simulations.

Publication VI: Production of defects in hexagonal boron nitride monolayer under ion irradiation,
O. Lehtinen, E. Dumur, J. Kotakoski, A. Krasheninnikov, K. Nordlund, and J. Keinonen, *Nuclear Instruments and Methods in Physics Research B*, in press, doi:10.1016/j.nimb.2010.11.027.

Ion irradiation induced defects in white graphene were studied in this publication by means of analytical potential molecular dynamics simulations. Akin to publication **IV**, impacts of He, Ne, Ar, Kr, and Xe ions were studied with energies ranging from 35 eV up to 10 MeV. The angle of incidence of the ion was included as an additional parameter as compared to

the setup in publication **IV**. The probabilities of producing different types of defects were reported, which can be used for optimizing ion processing of white graphene samples as well as for predicting the evolution of the material in radiation hostile environments.

Publication VII: Cutting and controlled modification of graphene with ion beams, O. Lehtinen, J. Kotakoski, A. Krasheninnikov, and J. Keinonen, *Nanotechnology* **22** 175306 (2011).

Ion irradiation induced defects in graphene were modeled using analytical potential molecular dynamics simulations. As in the case of white graphene presented in publication **VI**, the role of the angle of incidence of the ion was studied. Gallium was included in the list of simulated ions (a typical ion species used in focused ion beam systems) in addition to the noble gas ions used in the previous publications. It was observed that a high degree of selectivity over the produced types of defects could be obtained via careful selection of the irradiation parameters. To facilitate use of the large amount of data produced by the molecular dynamics simulations, a kinetic Monte Carlo code was developed for modeling morphological changes in a graphene monolayer under ion irradiation at macroscopic time scales and the code was made publicly available. This allows a direct comparison of experiments and simulations of ion irradiation of graphene. Moreover, the simulation code can be utilized when designing experiments on cutting graphene with focused ion beams.

2.2 Author's contribution

The author of this thesis carried out the ion irradiation experiments presented in publications **I**, **II**, and **III** and participated in the analysis of the results. In publication **V** the author participated in the development of the kinetic Monte Carlo model. In publications **IV** and **VII** the author carried out all of the molecular dynamics simulations and analysis of the results. In publication **VI** the author carried out major part of the molecular dynamics simulations as well as analysis of the results. In publication **VII** the author carried out the development of the kinetic Monte Carlo model. In publications **I** and **II** the author wrote the first drafts of the articles. In publications **III**, **V**, **VI**, and **VII** the author wrote the main body of the manuscripts except for the discussions on the Raman spectroscopy results in publication **III**.

3 Materials

Two closely related classes of materials, namely hexagonal carbon and boron nitride in their nano-incarnations are studied in this thesis. Carbon has been studied extensively due to its essential role in plethora of phenomena and applications in nature: Carbon is the primary building block of all living organisms, the ingredient which turns pure iron into steel and the sole species in carbon fibers, to name a few. Despite prolonged interest in this material, new exciting pages have been turned in the books of carbon during the latest decades with the advent of nanocarbon materials including fullerenes [31], carbon nanotubes [2–4], and graphene [1]. Due to the similarities in the atomic structures of carbon and boron nitride systems, similar nanostructures have since been predicted and discovered consisting of boron and nitrogen atoms [5–7]. The details of the synthesis of the materials are omitted in this thesis, but an interested reader can find further information on the matter, *e.g.*, in Refs. [32–34].

3.1 Bonding of atoms in carbon and boron nitride systems

As already introduced in elementary school, some atoms prefer sticking together under ambient conditions, which leads to the formation of molecules and solid state materials, in contrast to liquids and gases, where the constituent atoms move freely relative to each other.

The bonding of atoms into molecules and extensive crystal lattices is dictated by the way the valence electrons of the constituent atoms are redistributed when the nuclei are brought into the vicinity of each other. As a very crude description, one can say that if the electron density is concentrated between the nuclei, the positive nuclei are attracted towards the negative electrons and the atoms are bound together.

The question of how the electrons are distributed in a many-atom system is a quantum mechanical problem to which the exact solution for practically all systems, save the very simplest ones like H_2, is intractable. Throughout the 20th century many methods for finding approximate solutions to the problem have been developed and the work is continuing. In the case of molecules the molecular orbital theory is perhaps the most often employed approach, whereas density functional theory (DFT) is typically the tool of choice when describing crystalline solids.

Without going into further details of these methods (on DFT a more elaborate description is included in the *Methods*-section of this thesis), specific configurations of the nuclei can be found, in which the system finds its (local) energy minimum. These configurations can be characterized in terms of the number of bonds that are formed, in which geometries and how

strongly the system resists deformations of the ideal structure. These characteristics describe the mechanical structure and properties of the material. Moreover, insights into the electrical and magnetic properties of the material can be gained.

For carbon, two ordered macroscopic crystal structures are found in ambient conditions, namely the tetragonally arranged diamond structure and the hexagonally arranged graphitic phase, in addition to the randomly ordered amorphous carbon phase. These structures are shown schematically in Fig. 1 (a) and (b). Boron nitride exists as a hexagonally bonded structure practically identical to graphite in terms of atom locations, bond lengths (0.142 nm), and average atomic masses (12.01 amu for carbon versus 10.81 for boron and 14.01 for nitrogen) but with alternating boron and nitrogen atoms replacing carbon atoms, as shown in Fig 1 (c). Also boron nitride has other polymorphs including the sphalerite and wurtzite structures, which closely resemble the crystal structure of carbon diamond. In bulk graphite and hexagonal boron nitride layers of the planar structures shown in Fig. 1 (b) and (c) are stacked on top of each other bound together by the relatively weak van der Waals Force.

The two bonding configurations in carbon are often referred to as sp^2 and sp^3 bonding for hexagonal and tetragonal bonding respectively. This nomenclature stems from the valence band theory which can be used for describing bonding in molecules. Although the classical valence band picture of carbon bonding, related to hybridization of monatomic orbitals, is known to give inaccurate description of the localization of valence electrons at single and double bonds and so forth, the sp^n labelling scheme has remained as short hand for describing the different stable bond configurations.

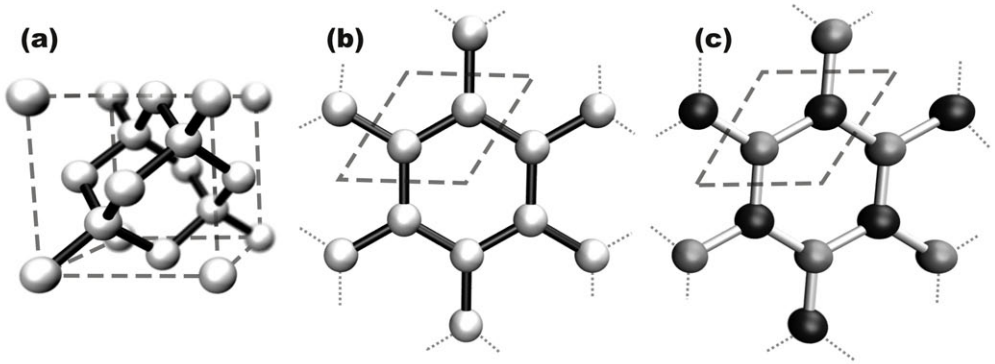

Figure 1: Tetragonal sp^3-bonding in the diamond unit cell (a) and hexagonal sp^2-bonding of carbon (b) and boron nitride (c). The white spheres represent carbon atoms, black spheres boron and gray spheres nitrogen. The sticks represent bonds between the atoms. The dashed lines denote the unit cells of the crystal lattices.

3.1.1 Differences between hexagonal carbon and hexagonal boron nitride

Although carbon and boron nitride closely resemble each other in terms of crystal structures, atomic masses and lattice constants, these materials are far from identical.

One difference is related to the possible modifications to the ideal structure of the materials. In this regard, carbon proves to be more versatile. This is illustrated in Fig 2. In the case of carbon, all the constituent atoms are identical and swapping two atoms obviously does not affect the energetics or stability of the structure. However, if neighbouring atoms in boron nitride are interchanged, *i.e.* a boron atom is replaced by a nitrogen atom and vice versa, we end up with two boron and two nitrogen atoms as nearest neighbours. In a hexagonal boron nitride lattice this kind of a configuration is not energetically favourable, which reduces boron nitrides ability to accommodate alterations introduced, *e.g.*, through radiation.

Non-hexagonal rings are often present in non-ideal sp^2 carbon materials [21]. For example, if one carbon atom is removed from a carbon hexagon, the remaining five atoms can form a pentagon and this structure is stable at moderate temperatures, although it imposes strain on nearby C-C bonds. In the case of boron nitride this is not the case, since any polygon with odd number of corners would require two atoms of the same species to be neighbours. This reduces boron nitride's ability to accommodate damage.

The nature of chemical bonding is sometimes described in terms of covalency and ionicity. In the case of covalent bonding, the bonded atoms share equally their valence electrons, which are concentrated in between the bonded atoms, due to which the atoms are attracted toward each other, as described earlier. In purely ionic bonding, one of the atoms captures the other's valence electron(s), thus rendering itself negatively charged and the other one positively charged, which again results in attraction.

Typically covalent bonds exhibit preferred directions of the bonds, resulting in structures such as the diamond and graphitic crystal lattices of carbon. The simple picture of ionic bonding, with a Coulombic force acting between positively and negatively charged ions does not imply any directionality in bonding and typically materials which are considered to be ionically bonded have close packed crystal structures such as the well known structure of sodium chloride with two inter-penetrating face centered cubic lattices.

In reality, the situation is not this simple, and often the nature of the bonds between atoms cannot be assigned in such strict categories. Boron nitride is an example of such a material. The crystal structures similar to carbon seem to imply covalent bonding between the constituent

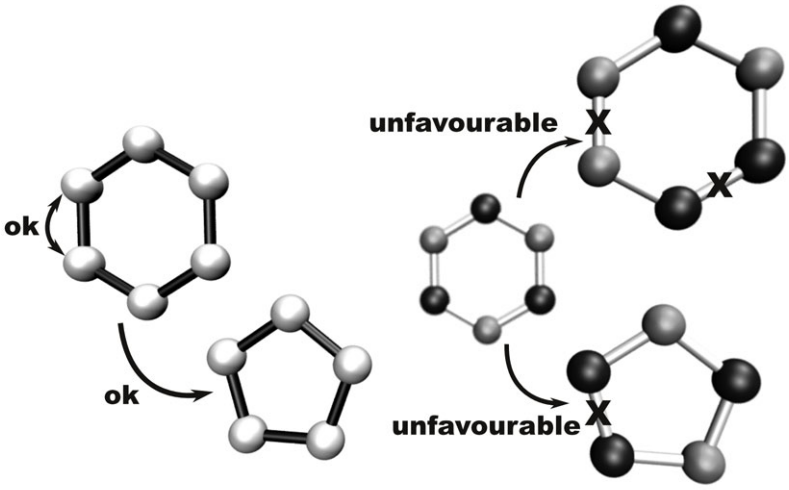

Figure 2: Examples of deviations from the ideal structure of sp^2 carbon and hexagonally bonded boron nitride. The rings are to be considered as parts of extensive crystal planes and not as isolated molecules. The white spheres represent carbon atoms, black spheres boron and gray spheres nitrogen. The sticks represent bonds between the atoms. The crosses mark unfavourable bonds in the boron nitride structures.

atoms, but on the other hand experiments and electronic structure calculations show that the valence electrons are in fact strongly localized around the nitrogen atoms [35,36], which in turn would imply ionic bonding. This, however, only underlines the shortcomings of the covalent-ionic categorization, and implies that hexagonal boron nitride falls somewhere on the middle ground.

The 'ionized' character of the boron and nitrogen atoms can however help in understanding why the nitrogen-nitrogen and boron-boron bonds are unfavourable in a defective hexagonal lattice, even though pure nitrogen forms N_2 molecules and many phases of pure boron exist [37]. When the atoms are part of the binary hexagonal boron nitride lattice, considerable charge transfer occurs, and atoms with a same signed net charge repel each other.

3.2 Graphene

Although graphene was the last one to be experimentally discovered of the known nanostructured phases of carbon [1], it is appropriate to treat it first, as it can be though of as the parent material of all the other structures, and knowing the properties of graphene helps in understanding the properties of the others.

The ideal structure of graphene is relatively simple: Graphene is an extensive sheet of carbon atoms connected to each other through sp^2 bonding, thus forming a two dimensional honeycomb lattice with a thickness of one atom, as schematically shown in Fig 3 (a). Graphene was experimentally isolated in 2004 [1], and K. S. Novoselov and A. K. Geim were awarded the Nobel price in physics for the discovery and for the subsequent research on the material.

It has been known for decades that graphite is made out of graphene sheets stacked on top of each other forming the familiar black bulk material. Thus the structure and properties of graphene have been the subject of many theoretical works dating back to as early as the 1940's [38], which can in part explain the rapid progress in graphene research. However, prior to the experimental discovery of isolated graphene, the emphasis was mainly on graphene as part of graphite.

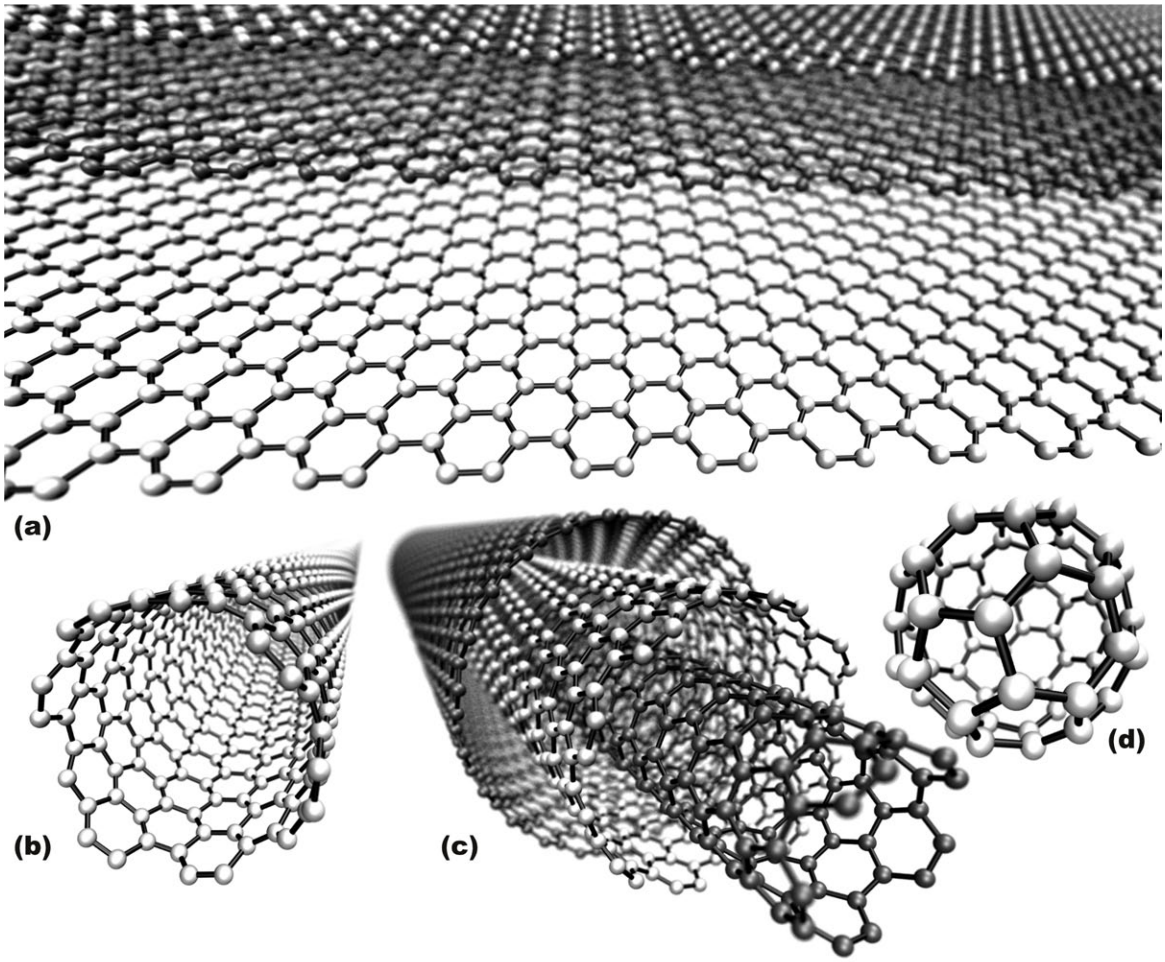

Figure 3: Ball and stick representations of the carbon materials studied in this thesis: (a) A graphene plane extending out of multilayer graphitic structure, (b) a single wall nanotube, (c) a multi-wall nanotube and (d) a fullerene (fullerene can be considered as the shortest possible nanotube structure). All the atoms are carbon.

3.2.1 Mechanical properties of graphene

The strong carbon-carbon bonds [39] along with the mechanically advantageous hexagonal ordering of the atoms grant graphene impressive mechanical properties. One should note though, that the mechanical properties of graphene are highly anisotropic, which stems from the anisotropic structure of graphene. When looking at the mechanical properties of graphene, it is important to understand that it is a true 2D material, so its strain energy density should be normalized by area rather than volume as in bulk materials. The resulting 2D values can be converted into bulk values by dividing them by the interplanar distance in graphite (0.335 nm). However, these converted values have a somewhat ambiguous meaning due to ambiguity in defining the thickness of the material, and should be used mainly to compare the properties of graphene to traditional bulk materials.

The mechanical properties of graphene stand out especially when the response to tensile strain in the in-plane direction is considered. Indentation measurements on a suspended graphene sheet have yielded values of 340(50) N/m for the 2D elastic modulus and 42(4) N/m for the 2D tensile strength, which correspond to bulk values of 1.0(1) TPa and 130(10) GPa respectively [40]. The elastic modulus matches well an experimental value obtained for highly oriented pyrolytic graphite in the in-plane direction (1.02(3) TPa) [41]. To put these values into context, corresponding values for steel are 200 GPa and 0.5–2.5 GPa. In other words, graphene is five times as stiff and two orders of magnitude stronger than steel. Hence, it is not difficult to imagine uses for such material, if graphene sheets can be manufactured with large area, good quality and low enough price, and some steps in this direction have already been taken [42–44].

One thing to keep in mind is that when compression is applied to graphene, the material is not stiff at all. This can also be attributed to the 2D structure, as nothing prevents buckling of the sheet to accommodate compression. Typically the impressive characteristics of graphene are not directly translated to bulk graphite either. The reason for this is the absence of covalent bonds between separate stacked graphene sheets in graphite. Only the weak van der Waals force holds the sheets together, thus allowing them to easily slip relative to each other (due to this graphite serves well as a mechanical lubricant and can be used as a pencil tip).

3.2.2 Electronic properties of graphene

In graphene two of the six electrons of a carbon atom are tightly bound in the lowest energy $1s$ state and these electrons do not directly participate in either bonding nor electrical conductance. Of the remaining four electrons three occupy the σ-band, which corresponds to the bonding

orbital holding graphene together. The last electron occupies the π-band and the structure of this band and the excited π^*-band govern the electrical conductance properties of graphene.

The most commonly cited approach to modelling the band structure of graphene is the tight-binging approximation first given by Wallace in 1947 [38]. A revised tight-binding approximation was described by Saito *et al.* in 1998 [45]. In this framework, the electronic structure is derived from a superposition of the basis functions of individual atoms (functions which describe the electronic structure of an isolated atom), where the overlap of the basis functions governs the transport of the π-electrons between sites and facilitates electrical conductance.

In this relatively simple treatment interactions between only the nearest neighbours are taken into account. This leads to a qualitatively correct description of the band structure. The most interesting part of the band structure is around the so called **K**-point (also called the Dirac point) in the Brillouin zone of graphene, where the valence and conductance bands meet. The tight binding approach reproduces this area well. The energy levels away from the **K**-point are not reproduced accurately, however, and more sophisticated approaches are required to correctly model the band structure in those areas, such as tight-binding models taking also second and third nearest neighbours into account [46] or *ab initio* calculations directly.

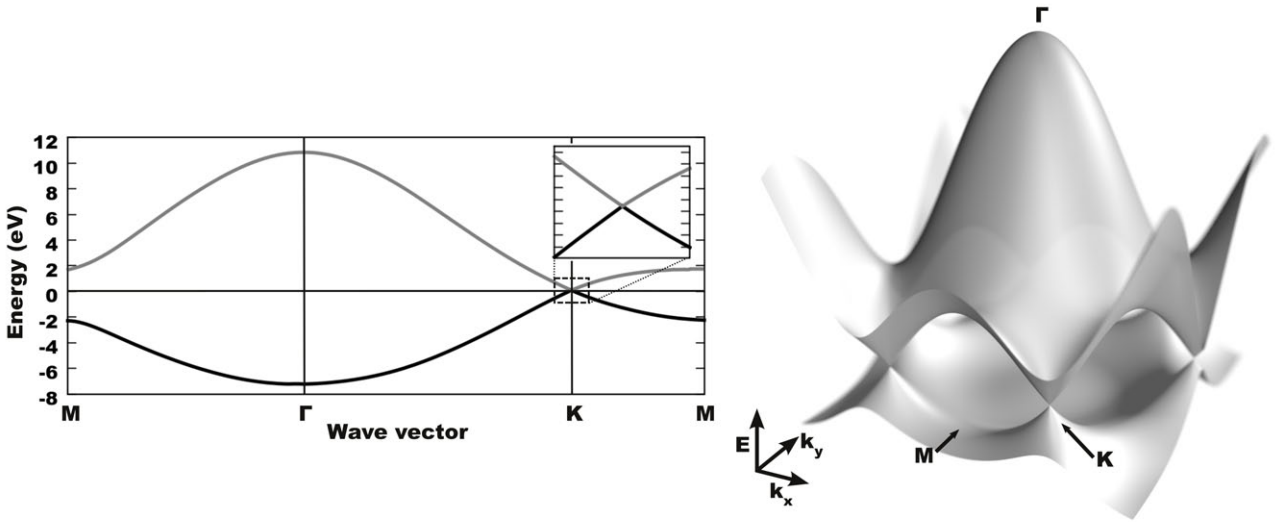

Figure 4: Schematic plots of graphene's valence and conductance π and π^*-band structure between the high symmetry points **Γ**, **K** and **M** inside the first Brillouin zone of graphene (left) and as a 3D plot (right).

Plots of the band structure are shown in Fig. 4. As was mentioned above, the region around the **K**-point is of particular importance. First of all, the valence and conductance bands touch there, which means there is no band-gap, meaning that electrons can be easily excited to the

conduction band at finite temperatures. However, the density of states at the band-gap is zero, which makes the classification of graphene in the metal-semiconductor-insulator scheme somewhat ambiguous. Indeed, graphene is often referred to as a semi-metal or a zero-band-gap semiconductor. Nevertheless, no excitation energy is required to move an electron from the valence band to the conductance band.

Another curious feature of the band structure near the **K**-point is the linear slope of the bands. In 'typical' materials the dispersion relation is quadratic, leading to non-zero effective masses of the charge carriers. In graphene, however, the linear dispersion relation leads to vanishing effective mass. In general, a particle is called ultrarelativistic when its speed is very close to the speed of light. In this case the energy of the particle ($E^2 = m^2c^4 + p^2c^2$) can almost completely be attributed to its momentum ($E \approx pc$). If the π-band structure of graphene is expanded close to the **K**-point ($\mathbf{k} = \mathbf{K} + \mathbf{q}$ and $|\mathbf{q}| \ll |\mathbf{K}|$), one obtains

$$E_{\pm}(\mathbf{q}) \approx \pm v_F|\mathbf{q}| + O[(q/K)^2] \tag{1}$$

where v_F is the Fermi velocity, $v_F \simeq 10^6$ m/s [16]. The implication of this result is that the π-electrons behave like ultrarelativistic particles, but with the speed of light c replaced by the Fermi velocity. Experimental evidence of this phenomenon can be found in Refs. [47–50].

3.3 Carbon nanotubes

A carbon nanotube is a cylindrical molecule consisting solely of sp^2-bonded carbon. One can imagine constructing a carbon nanotube by cutting a straight strip out of a graphene sheet and rolling it into a tube. The direction in which the strip is cut defines the chirality of the nanotube. A schematic representation of such a structure is shown in Fig. 3 (b). This kind of a nanotube is called a single-walled carbon nanotube (SWCNT) for obvious reasons. Often nanotubes do not come in the single-walled form, but are made out of multiple concentric shells as is depicted in Fig. 3 (c). Such nanotubes are called multi-walled carbon nanotubes (MWCNT). Additionally, a fullerene is presented in Fig. 3 (d), as nanotubes are often capped by fullerene like half-spheres consisting of hexagonal and pentagonal carbon rings.

There is no clear consensus on who should be credited for the discovery of carbon nanotubes [51]. The first reported experimental observations of carbon nanotubes are from 1952 by Radushkevich *et al.* [2]. In 1976 Oberlin *et al.* showed hollow carbon fibers with nanometer-scale diam-

eters and a TEM image of a nanotube consisting of a single wall of graphene [3]. Evidence of carbon nanotubes has also been presented by Hillbert *et al.* [52] and Abrahamson *et al.* [53]. In 1991 S. Iijima presented his observations of "Helical microtubules of graphitic carbon" [4], which sparked widespread interest in carbon nanotubes.

3.3.1 Mechanical properties of carbon nanotubes

The impressive mechanical properties of graphene are readily translated to those of carbon nanotubes. Calculations [13,39,54,55] predict the Young's modulus of a defect-free single-walled carbon nanotube to be $\sim$1 TPa, tensile strength >100 GPa, and strain at failure 15–30%.

Peng *et al.* conducted direct stress-strain measurements on individual high quality MWCNTs and acquired tensile strengths and Young's moduli close to the theoretically predicted values (>100 GPa and >1 TPa respectively) [8]. Earlier experiments had yielded Young's moduli in the range of $0.27 - 0.95$ TPa and tensile strengths from 11 to 63 GPa [11]. The differences in the values can be explained by defects in the tested nanotubes. Krishnan *et al.* obtained a value of 1.3(5) TPa [56] for the Young's modulus of an individual SWCNT and Wei *et al.* obtained a value of 1.7(9) TPa [57]. Both measurements were based on tube vibrations. Wang *et al.* conducted tensile tests on individual SWCNTs in an electron microscope and acquired tensile strengths ranging from 25(3) to 102(13) GPa depending on the tested tube, with the lower values again attributed to structural defects in the tubes [14].

The easy slippage of carbon nanotubes relative to each other in both MWCNTs and SWCNT bundles (SWCNTs have a strong tendency to stick together in bundles because of a van der Waals interaction and large surface area) hinder seriously the utilization of the individual tube's superior mechanical properties in real applications. Kis *et al.* were able to considerably improve the situation by introducing defects in SWCNT bundles using electron irradiation [10]. The individual tubes formed covalent bonds at the defect sites, thus making slippage more difficult and gained a 30-fold increase in the bending modulus of the bundle. Peng *et al.* irradiated MWCNTs with electrons and observed up to 11.6-fold improvement in the maximum sustainable loads, explained by irradiation-induced crosslinking of the separate walls of the tubes [8]. Similar treatment has been proposed using ion irradiation [15, 58].

3.3.2 Electronic properties of carbon nanotubes

The π-band structure of a SWCNT can be constructed by starting from the band structure of graphene in the zone-folding scheme [45]. The continuous allowed **k** values in the Brillouin zone of graphene are cut by parallel and equidistant lines, as sketched in Fig. 5. **k** values in a nanotube can only reside on these lines. The transformation of the band structure from a 2D surface to a series of 1D curves stems from the transformation of the 2D graphene structure to the essentially 1D structure of a nanotube. The multiple parallel lines are present due to the rotational periodicity of the nanotube structure relative to the nanotube axis.

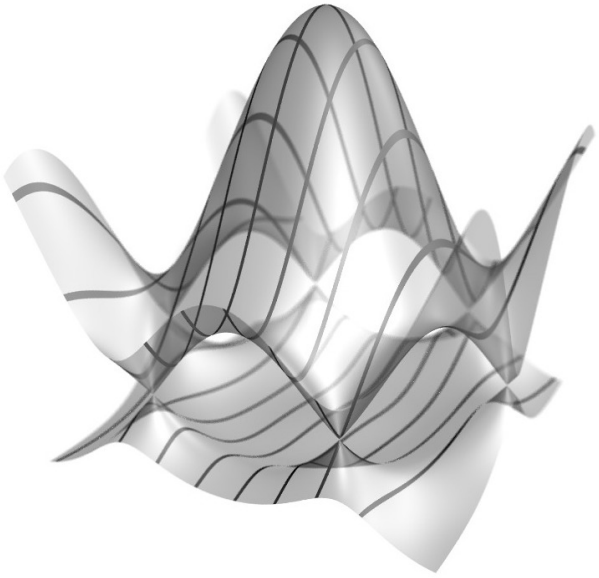

Figure 5: Schematic representation of the π-band structure of a single-wall nanotube. The surfaces are the π and π^*-bands of graphene and the lines mark the allowed states of a certain nanotube.

A single-walled carbon nanotube can be of metallic or semiconducting character. This is governed by the direction in which the rolled up nanotube is 'cut' from a sheet of graphene (in reality nanotubes are not synthesized by actually cutting and rolling graphene, but this idea helps in understanding the structure). This direction dictates the direction of the cut-lines in the band structure. Only with cut-lines in certain orientations, graphene's **K**-point is included on the line and only in these cases the nanotube has a zero band-gap, which renders the tube metallic. Otherwise the nanotubes are semi-conducting. The shells of MWCNTs are not necessarily correlated in terms of being metallic or semiconducting. However, there is a high probability of having metallic tubes included in the selection of walls of any MWCNT. Again it should be noted, that the tight-binding approach does not reproduce correctly the details of the band-structure, but does give a proper qualitative description [46].

3.4 White graphene

White graphene, *i.e.* a monolayer of hexagonal boron nitride (*h*-BN), has similar structure to graphene (see Fig. 3 (a)), but with alternating boron and nitrogen atoms substituting for carbon

atoms, as shown in Fig. 1. Also, similar to graphite, bulk *h*-BN consists of *h*-BN monolayers stacked on top of each other. Due to the partial ionicity of the B and N atoms in the lattice, the layers prefer to be aligned so that alternating positive B and negative N atoms are superposed on top of each other [32].

Since the discovery of graphene, great interest in producing monolayers of *h*-BN has risen. Research on epitaxial monolayers on metal surfaces has been conducted earlier as well [59–61], and contrary to epitaxial graphene, the boron nitride monolayers were observed to be only weakly physisorbed to the substrate, which means that the measured properties reflected those of isolated monolayers.

Production of isolated white graphene has proven difficult. This is mainly due to stronger interlayer interactions in *h*-BN as compared to graphene [32]. The partially ionic character of the constituent atoms results in a relatively strong attraction between the layers. Hence, formation of double and triple layers is preferred. In 2009 Jin *et al.* [6] and Meyer *et al.* [7] were able to produce freestanding white graphene, by first producing flakes with a limited number of layers (10 or less), *e.g.*, by the procedure reported in Ref. [62] and subsequently thinning down the membrane to ultimately a single layer via *in situ* sputtering in an electron microscope. Other groups have also reported ultrathin *h*-BN [62–70]

3.4.1 Mechanical properties of white graphene

Due to the difficulty of producing samples of isolated white graphene, direct measurements of the mechanical properties of this material have not been reported so far. Green *et al.* made theoretical predictions of the elastic properties of *h*-BN [71] and reported a value of 1.04 TPa as the Young's modulus and 31.4 GPa as the bending modulus. Li *et al.* measured the bending moduli of thin multilayered *h*-BN samples using an atomic force microscope and acquired values ranging from ∼18 GPa for thicker samples (thickness > 100 nm) and increasing to ∼27 GPa for samples of thickness 25 nm (70-80 *h*-BN layers) [68] approaching the theoretical value given by Green *et al.*. The lower values for the thicker samples was attributed to increased probability of having defects and stacking faults when the number of layers is higher.

The theoretically predicted value for the Young's modulus of *h*-BN (1 TPa) matches that of graphene's, which is not that surprising, if one considers the similarity of their structures. Obviously, there is a lot of room for experiments regarding the mechanical properties of white graphene, but from the analogy with graphene, one can assume them to be of the same order of magnitude to those of graphene, especially close to equilibrium.

3.4.2 Electronic properties of white graphene

When it comes to electronic properties, white graphene differs greatly from graphene: White graphene is a wide gap semiconductor or an insulator, depending on where the line is drawn. The width of the band-gap has not been reported on (according to bibliographic searches by the author) for an isolated monolayer. Experimental values for the band-gap of bulk *h*-BN have quite a large variation ranging from 3.6 [72], 4.02 [73], 5.97 [74] to 6.0 eV [75]. Nagashima *et al.* measured the band-gap of a *h*-BN monolayer physisorbed on metal substrates and acquired values of 3.6, 4.0 and 4.9 eV on Ni(111), Pd(111) and Pt(111) substrates respectively with a direct band-gap at the **Γ** point of the Brillouin zone. Ooi *et al.* calculated the width of the band-gap using density functional theory (DFT) and acquired values ranging from 4.54 eV to 4.58 eV depending on the approximations used [36] (however, one should be cautious when dealing with band-gap values evaluated through DFT [76]). Blase *et al.* reported a value of 6.0 eV obtained using DFT and based on the GW approximation [77], which typically reproduces experimental semi-conductor band-gap values accurately [78].

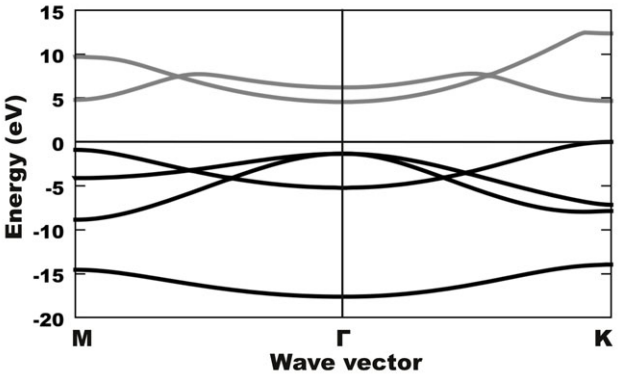

Figure 6: Band structure of white graphene through selected symmetry points in the hexagonal Brillouin zone, courtesy of Jani Kotakoski.

Overall, although the numerical value of the band-gap is not unambiguously established or even whether *h*-BN has a direct or indirect band-gap, it is clear that a relatively wide band-gap exists and ultrarelativistic Dirac fermions and other graphene's peculiarities are absent in white graphene.

3.5 Boron nitride nanotubes

Boron nitride nanotubes (BNNT) are analogous structures to carbon nanotubes, but with alternating boron and nitrogen atoms again replacing carbon atoms similar to the the case of graphene and white graphene (see Fig. 7). Multi-walled BNNTs were first synthesized by Chopra *et al.* in 1995 [5], one year after they were theoretically predicted [79]. Single-walled BNNTs have been observed more seldom than SWCNTs [80], which can be explained again by

the stronger interaction between adjacent *h*-BN sheets, which makes a multi-layered structure energetically favourable.

A BNNT can be rolled from strips cut in practically arbitrary directions from white graphene again similar to carbon nanotubes and BNNTs of many chiralities have been observed. However, majority of observed BNNTs are of 'zig-zag' type (such a tube is shown in Fig. 7, where the open edge forms a 'zig-zag' pattern) [32]. This feature is different from standard carbon nanotubes, where no specific chirality is preferred. Also in multi-walled BNNTs all the layers of an individual tube tend to have similar chiralities, which makes it possible to have as many as possible B-N pairs stacked on top of each other [32]. Further on, the preference to have B-N pairs aligned between adjacent tube shells results in multi-walled BNNT's cross-section to be polygonal, rather than circular as in the case of MWCNTs [81].

Another deviation from the structure of carbon nanotubes in the case of BNNTs is the typical tube cap structure. A spherical fullerene-like cap structure would require the presence of odd-numbered atom rings. This kind of a structure would lead to B-B and N-N pairs, which is not a stable configuration, as was discussed earlier. A typical non-hexagonal ring in a *h*-BN based structure has instead four members (such rings are shown in the model of a $B_{12}N_{12}$ fullerene in Fig. 7). This kind of a topological 'defect' leads to BNNTs having flat tips with right-angle corners [32].

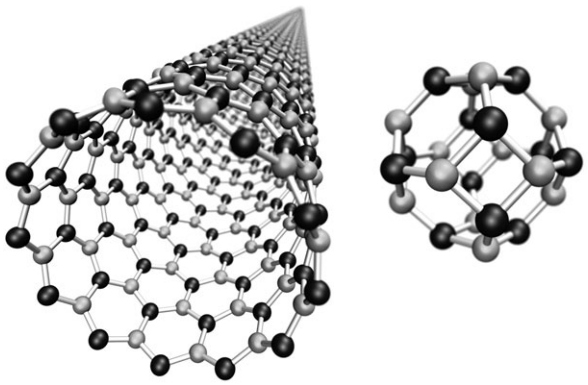

Figure 7: A zig-zag boron nitride nanotube and a $B_{12}N_{12}$ fullerene. The black spheres represent B atoms and gray spheres N atoms.

3.5.1 Mechanical properties of boron nitride nanotubes

Since the mechanical properties of white graphene seem to rival those of graphene, it can be expected that BNNTs have comparable properties with carbon nanotubes. In fact, the Young's modulus of a BNNT has been theoretically predicted to be ∼0.9 TPa [82]. Chopra *et al.* performed vibration amplitude and frequency measurements on multi-walled BNNTs [83] (similar to what Treacy *et al.* had conducted on MWCNTs [84]) and acquired a Young's modulus of 1.2(3) TPa. Golberg *et al.* performed bending force measurements using an atomic force microscope integrated to a high resolution transmission electron microscope and reported

Young's moduli of $0.5 - 0.6$ TPa [81]. Interestingly, when the BNNTs were bent enough, sharp kinks were formed and the tube was folded around these points, but as the bending stress was released, the tube fully restored its original structure.

Direct tensile tests of multi-walled BNNTs were performed by Wei *et al.* [85]. In these experiments the Young's modulus was observed to vary from 0.7 to 1.3 TPa for various tubes. The tensile strengths were measured to range from 16.5 to 33.2 GPa. Contrary to MWCNTs, where typically the outer shell slides easily over the inner ones after yielding under tensile stress, the BNNTs showed only minor sliding after shell breakage, after which another shell became the load-bearing part, ultimately leading to breakage of all of the shells. As was described above, BNNTs have typically polygonal cross-sections and the shape of the cross-section changes along the length of the tube, which prevents easy sliding of the walls relative to each other according to Wei *et al.* [85].

3.5.2 Electronic properties of boron nitride nanotubes

Similar to bulk *h*-BN and white graphene, BNNTs have a wide band-gap. The band-gap has been theoretically estimated to be $\sim$5 eV, except for tubes with very small diameter, where the band-gap has been predicted to decrease to $\sim$2 eV in tubes with a diameter of $<$1 nm [86]. However, no experimental reports on such small tubes could be found by the author. The width of the BNNTs band-gap does not depend on the chirality of the tube, contrary to carbon nanotubes, although whether the band-gap is direct or indirect can be affected [79]. As is the case with white graphene and contrary to carbon nanotubes, BNNTs are insulators.

3.6 Defects

Above, the discussion on the properties of the studied materials has focused on perfect non-defective structures. However, defects can be introduced (intentionally or unintentionally) into any material and these often have a profound influence on practically all of the properties of the material.

The work presented in this thesis concentrates foremost on intrinsic defects, meaning defects where no foreign atoms are introduced in the system. Rather, deviations from the initial structure (either pristine as synthesized materials in the experiments, or non-defective structures in the theoretical works) are considered. Some examples of such defects are presented in Fig. 8 for the case of graphene. Similar types of defects can also be found in nanotubes and

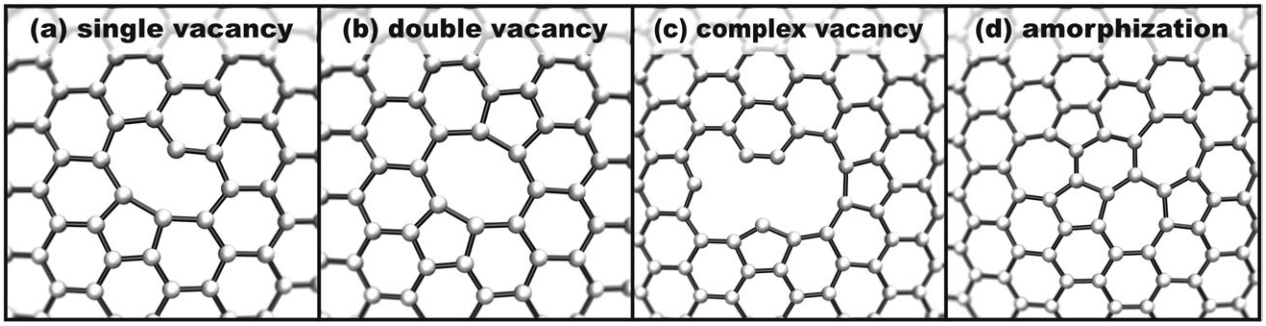

Figure 8: Examples of point defect configurations in graphene. The nomenclature is the same as was used in publications **VI** and **VII** in this thesis. A single vacancy is a defect structure, where one carbon atom is missing from otherwise intact structure, a double vacancy has two missing atoms from otherwise intact structure, a complex vacancy is any defect with missing atoms other than single or double vacancy and amorphization is a defect structure with no missing atoms. Defects in white graphene can be classified in similar fashion, but with the addition of separate B and N vacancies.

white graphene, although it should be noted that the odd-numbered rings are not necessarily energetically favourable in *h*-BN due to the unfavoured bonds between atoms of the same species. However, two boron atoms can form a bond at the edge of a vacancy, similar to Fig. 8 (a) [87,88]. Also, in experimental conditions, where non-zero concentrations of reactive species such as hydrogen or oxygen can be present, the dangling bonds (*e.g.*, a carbon atom with only two neighbours in a defective hexagonal network is said to have a dangling unsaturated bond) can be saturated with foreign species quickly after the creation of the defect.

In the case of graphene, deviations from the perfect hexagonal network alter the electronic structure. New quasilocalized electron-states are introduced around the Fermi level of graphene [89–91]. In terms of electrical conductance, defects disturb the propagation of electron waves by acting as scattering centers [16], hence lowering the conductance, much like in ordinary bulk materials.

The zero band-gap of perfect graphene presents some challenges when building electronic components is considered. One such problem is a low on-off ratio of graphene based transistors [92]. If a graphene sheet is narrowed down in one direction to form a so-called nanoribbon, a band-gap can be opened, depending on the orientation of the hexagonal lattice in the ribbon and structure of the edges [16, 17]. Such band-gap opening has been exploited to construct field effect transistors out of graphene with a high on-off ratio [93]. Alternatively quantum dots can be carved out of graphene, where a small graphene island serves as the quantum confinement. Such a construction has been demonstrated to work as a transistor with a high on-off

ratio [18]. Further on, graphene anti-dot lattices, where a periodic lattice of holes is introduced into graphene, have been shown to be another route to graphene based electronics [19, 20].

The presence of uncompensated vacancies (where vacancies in only one of two sublattices of graphene are present, with a single vacancy being the simplest case) can lead to opening of a band-gap with quasilocalized zero modes at the Fermi level, which in turn can lead to formation of local magnetic moments [89, 90, 94–96]. Ferromagnetism with Curie temperature well above room temperature has been experimentally observed in defective sp^2 carbon structures, such as graphite [97–99], polymerized fullerenes [100], hydrogenated carbon nanotubes [101], nanodiamonds [102] and graphene [103]. However, another study [104] found no trace of ferromagnetism in graphene nanocrystals obtained by sonic exfoliation, which are not expected to be defect free and have large portion of the carbon atoms located at edges due to the small size of the individual graphene flakes. Hence, the magnetic properties of defective graphene remains a subject requiring further studies.

No experimental data on the influence of defects on the mechanical properties of graphene could be found by the author. Grain boundaries have been estimated to reduce the tensile strength of graphene, with the size of the reduction depending strongly on the direction of the grain boundary and the orientation of the grains relative to each other [105]. However, mechanical properties of defective carbon nanotubes have been studied extensively, and the results can be assumed to be indicative of how graphene would be affected by defects. In carbon nanotubes, point defects have been observed to decrease the Young's modulus and tensile strength considerably [11–14]. The presence of vacancy type defects can contribute in superplastic deformation of carbon nanotubes [106, 107], where a SWCNT can be elongated three-fold and shrunk fifteen-fold in diameter under tensile strain at elevated temperatures [108].

The electrical resistivity of carbon nanotubes rises rapidly if defects are introduced, as demonstrated in ion irradiation experiments on individual SWCNTs [26] and SWCNT bundles [109]. Theoretical treatments also provide evidence for this [110]. However, point defects can act as gate-tunable electrons scatterers in metallic SWNTs, which can be taken advantage of when designing new types of electronic devices [111]. An intratube quantum dot formed by two defects has in fact been reported [112].

Further advantageous effects of defects observed in carbon nanotubes are enhanced field emission [27, 113] and mechanical strengthening of nanotube bundles [10, 114], MWCNTs [8] and bulk nanotube samples [15, 115].

The electronic properties of pristine white graphene are not as exciting as those of graphene due to the wide band-gap. Defective white graphene can have some interesting properties, however. Vacancy type defects can introduce localized states near the Fermi-level depending on which atom species are removed [22, 116]. This can result in narrowing of the band-gap, or even half-metallic spin-polarized conduction. Boron single vacancies have been estimated to have net magnetic moments [22] as well as double vacancies of various types [116]. A zig-zag edge of a white graphene flake has been calculated to be metallic [117] and the band-gap of a zig-zag edged white graphene nanoribbon to converge to a value 0.7 eV [23] lower than the bulk gap with decreasing width of the ribbon. An external transverse electric field can further lower the band-gap of a white graphene nanoribbon and ultimately reach a zero-gap state [24].

The formation energies of bond-rotation types of defects in BNNTs are higher than in carbon nanotubes, which can lead to higher failure resistance under tension [118] (rotations of bonds in nanotubes is required for plastic deformation). This, however, means that BNNTs can be more brittle under tension [119]. No direct studies on the effects of vacancy type defects on the mechanical properties could be found by the author, but it can be assumed, that the mechanical properties are adversely affected, especially as reconstruction of the hexagonal network in BNNTs is more difficult than in carbon nanotubes.

h-BN structures are highly inert chemically, which can be a great asset [120], since for example during purification of synthesized nanotubes less defects are produced, leading to better mechanical properties as compared to their carbon counterparts. This can be problematic though, if chemical functionalization is desired. Here intentionally induced defects, *e.g.*, through ion irradiation, can be helpful as the under-coordinated atoms around defects are more prone to chemical reactions (this also applies to the carbon structures).

4 Experimental methods

Publications **I-III** of this thesis report experimental studies, in which MWCNT and multi-walled BNNT samples were irradiated with energetic ions. The induced changes were characterized using transmission electron microscopy and Raman spectroscopy. The author of this thesis conducted all of the ion irradiations, whereas colleagues operated the characterization apparatuses. Below the employed experimental methods are reviewed.

4.1 Ion irradiation

The first particle accelerators were built in the early 20th century, but for a long time they were exclusively used by nuclear physicists. However, in the latter half of the century accelerators found lots of uses in the materials sciences, ranging from analysis techniques to controlled modification of materials properties, with doping of silicon in semiconductor device manufacturing being probably the most important application.

Figure 9: The 500 kV ion accelerator at University of Helsinki. Photo courtesy of Jani Kotakoski.

The basic principle of ion beam modification of materials is quite straightforward: Energetic ions collide with the target atoms and can both displace the atoms and get stuck in the material as impurities. The former can be used to introduce well defined disorder in materials for further studies of the effects of the defects on the properties of the materials [26, 27] or to produce structures with nanometerscale features [25, 29, 30, 121].

In the work presented in this thesis, ion irradiation was used to produce defects in multi-walled carbon and boron nitride nanotubes, which were later on characterized using other techniques. All of the ion irradiation treatments presented in this thesis were conducted at the Division of

Materials Physics at the University of Helsinki. The accelerator used was a 500 kV air insulated ion implanter system manufactured by High Voltage Engineering Europa B.W.

In the accelerator, the ions are produced in a cold cathode penning ion source from gas phase materials, where an electrical arc discharge is sustained inside a low pressure cavity, which ionizes the components of the gas. A voltage of $10 - 30$ kV is used to extract and accelerate the ionized species through a small aperture in the cavity. This particle stream is fed through an analyzing magnet, which can be used to select the desired mass to charge ratio from the diverse ion selection produced by the ion source.

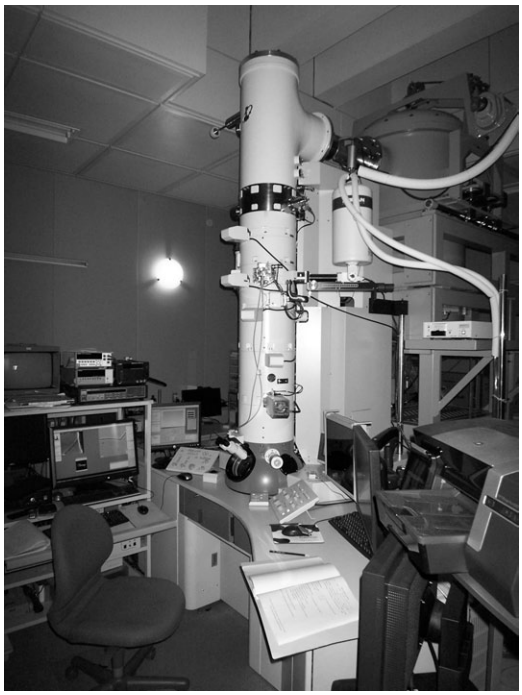

Figure 10: A transmission electron microscope at National Institute for Materials Science, Tsukuba, Japan.

After the analyzing magnet, the ions are directed into an electric field generated by a solid state multi-doubler stack of $0 - 500$ kV. This electric field accelerates the ions into an energetic ion beam. Various magnetic and electrostatic ion-optical instruments are employed to manipulate the path of the ion beam as well as to ensure correct focusing.

In order to achieve a homogeneous irradiation treatment of a target, the ion beam is run through a beam sweeping system, which rasterizes the beam across the desired area. Faraday cups with a known cross-section are placed inside the exposed area and the accumulated charge is measured, from which the number of ion impacts per unit area can be determined.

Beyond the ion source, the ion beam is run in vacuum in order to prevent undesired scattering of the ions from atmospheric particles as well as to prevent sample contamination. The vacuum is created and maintained using turbomolecular high vacuum pumps assisted by rotary vane and scroll pumps. A typical vacuum level of the system is $< 10^{-7}$ mbar when the ion beam is not present. If a high intensity beam is used, the vacuum level can deteriorate by an order of magnitude, as particles are constantly introduced into the system via the ion beam.

4.2 Transmission electron microscopy

Transmission electron microscopy (TEM) in its simplest form is not much different from optical microscopy. Where 'normal' lenses and mirrors are used to form an image from photons in optical microscopy, TEM is based on making images using an electron beam instead of light, and applying magnetic components for focusing and other electron-optical purposes.

The first TEM was built by Max Knoll and Ernst Ruska in 1931 [122], for which Ruska was awarded the Nobel price in 1986, which underlines the importance of this invention in both materials and biological sciences. The main advantage of using electrons instead of photons for imaging is the orders of magnitude shorter de Broglie wavelength of electrons as compared to photons. The shorter wavelength translates directly to better ultimate resolution. In fact, even individual atoms can be observed with modern TEM systems. TEM has been an essential tool in the progress of modern nanoscience and many of the discoveries would not have been possible without it.

In the work presented in this thesis, three TEMs were used. The MWCNT samples were imaged using a HR-TEM FEI Tecnai F-30 with a field emission gun and an acceleration voltage of 300 kV, In the case of BNNTs, TEM imaging was conducted using a 300 kV HR field-emission TEM JEM3100FEF (JEOL) equipped with in-column Omega Filter. The white graphene imaging was conducted using an aberration-corrected TEM (JEOL 2010F) with acceleration voltages of 80, 120, and 200 kV.

4.3 Raman spectroscopy

Raman spectroscopy is a technique, in which inelastic scattering of monochromatic light (usually from a laser) is used to study vibrational, rotational and other low-frequency modes in a system [123]. The technique is named after one of its discoverers, Sir C. V. Raman, who was also awarded the Nobel Prize in Physics in 1930 for the discovery.

In Raman spectroscopy, a laser beam is pointed at a sample and shifts in the wave length of the scattered light are observed. The incident light is scattered by the target atoms or molecules. In the scattering process, the target system is excited to a 'virtual' or unstable energy level and it quickly relaxes to either the ground state (Rayleigh scattering) or an excited vibrational or rotational state (Raman scattering). The energy difference of the starting and finishing states is manifested as energy shifts of the scattered light. From the intensities of these shifts information on the structure of the target material can be deduced.

Raman spectroscopy has proven to be a useful tool in characterizing disorder in carbon based materials [124–127]. In the case of sp^2 bonded carbon, a dominant Raman shift is located at $\sim$1580 cm^{-1}, which is generally referred to as the G-band ("graphite" band). If the perfect structure of a graphitic plane is disturbed, *e.g.*, defects are introduced, another band, typically termed as the D-band ("disorder" band), is introduced somewhere between 1280 and 1400 cm^{-1} depending on the laser wavelength [128, 129]. The relative intensities of the G and D bands can then be used to characterize the amount of disorder in a carbon sample.

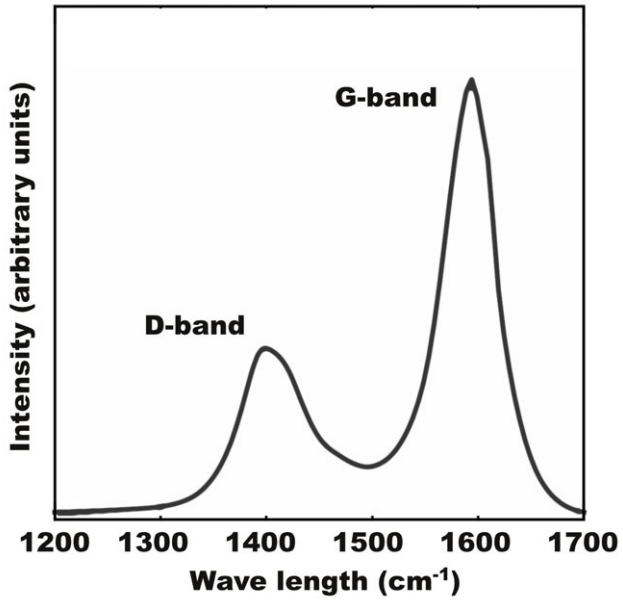

Figure 11: A schematic of a Raman spectrum originating from slightly defective sp^2 carbon structure showing the G-band originating from intact areas and the defect related D-band.

In publications **I**, **II**, and **III** two setups were used for Raman spectroscopy. The first setup consists of an Ar ion laser (514.5 nm, Omnichrome 543-AP), a single-stage spectrometer (Acton SpectraPro 500I, resolution 3 cm^{-1}), and a CCD camera (Andor InstaSpec IV). The second one is a LabRam confocal microscope (HR 800 Jobin Yvon) using excitation at 488 nm of an Ar ion laser (< 0.5 mW on sample), 50x and 100x objectives and spectral resolution 2 cm^{-1}.

5 Theoretical methods

In science, nature gives the final answers and ultimately carefully executed experiments are the way of posing our questions. However, theoretical analysis of phenomena have always been at the core of scientific thinking and progression, as insights into underlying reasons of the observed phenomena and predictions on their consequences can be drawn by constructing models describing the observations. Further experiments can in turn be conducted to test the soundness of the theories, and so a dialogue between the two aspects of science proceeds.

When constructing a theoretical model of a real physical phenomenon, approximations are *always* needed. No system is ever completely isolated from the surrounding world and mechanisms of the interactions both within and outside of the studied system comprise of such an complicated intertwined network, that nothing else but nature itself can replicate it. Thus correct and well justified choice of approximations lays at the center of physical models. This

choice on one hand dictates the level of detail that the model can replicate, but on the other hand very much governs the scope of the predictions of the model: Often the more detail is abstracted away through approximations, the larger a picture can be painted.

In the work presented in this thesis, computational methods founded on different levels of abstractions are employed. Density functional theory is employed for modeling the energetics of atomic scale displacements in the studied materials, analytical potential molecular dynamics simulations are used to investigate the irradiation response of the studied materials to a wide selection of ions and energies and Monte Carlo simulations are used to study the long time evolution of the studied materials under continuous particle bombardment.

5.1 Molecular dynamics

Molecular dynamics (MD) is a simulation method, where the equations of motion of a large number of particles are solved numerically, with a given model of interaction between the particles [130]. One key approximation typically employed in such simulations, is the Born-Oppenheimer approximation [131], in which it is assumed that the nuclei are moving so much slower than the surrounding electrons, that the electron system has enough time to find its ground state for each spatial configuration of the nuclei. Thus the forces acting on the nuclei can be described based solely on the spatial configuration of the nuclei and independent of their velocities[2].

Molecular dynamics was developed by Alder and Wainwright in the 1950's for studying phase transitions and atomic vibrations in molecules [132–134] and continues to be a central tool when atomic scale behaviour of matter is studied. The rapid increase in computing power during last decades has rendered the method ever more powerful and more and more complex problems have been brought within its reach.

5.1.1 Analytical potential MD

The interaction of nuclei and electrons in matter has a fundamentally quantum-mechanical nature and these interactions can be evaluated at the quantum-mechanical level (see the section *Density functional theory* below), but this is computationally a very expensive operation and

[2]Although electrons are not directly modeled in analytical potential MD, the Born-Oppenheimer approximation is implied by the fact that the interaction potential is not affected by the earlier time evolution of the system.

constraints in computer power and available wall clock time limit the applicability of such precise approach to rather small systems and limited number of simulations.

In analytical potential (AP) MD the quantum mechanical interactions of the atoms are approximated by analytical functions, which are constructed and parameterized to reproduce the forces of interaction, crystal structure, bond lengths *etc.* of the species in question as compared to *ab initio* calculations and/or experiments. If such a function can be constructed and employed, the computational efficiency of MD simulations is increased considerably as compared to *ab initio* calculations. Indeed, hundreds of atoms can be studied based on *ab initio* calculations directly, but AP MD simulations can handle even millions of atoms.

The reliability of the results produced by AP MD simulations is bound by the reliability of the used potential function, and the results should always be approached with proper caution. As a relevant example, in the publications **IV**, **VI** and **VII** analytical potentials are employed in mapping the ion irradiation response of monolayer targets. In these studies statistical predictions on defect sizes are made after a large number of simulated events. The predictions most of all depend on the energetics of displacing atoms, and directions and velocities of recoiled atoms after collisions, which can be verified based on *ab initio* calculations and basic kinetics of elastic collisions.

The most simple form of an analytical interaction model is a pair potential, where only interatomic distances of individual atom pairs dictate the potential energy of the system. The Lennard-Jones [135] and Morse [136] potentials are well known examples of pair potentials and can describe quite accurately noble gases and diatomic molecules, respectively. Typically a pair potential can be written as

$$V(r) = V^R(r) - V^A(r), \tag{2}$$

where r is the interatomic distance and $V^R(r)$ and $V^A(r)$ are the potential's repulsive and attractive parts, respectively. In general the functional forms of the repulsive and attractive forms are such, that at short distances the repulsive part outweighs the attractive, in order to model Pauli repulsion due to overlapping electron orbitals and Coulomb repulsion of the nuclei. At long distances the attractive part dominates, and somewhere in between lies a potential energy minimum corresponding to the non-strained bond length.

Another example of a pair potential is the Ziegler-Biersak-Littmark universal repulsive potential [137], which is used to model the repulsive interaction of the energetic ions and target atoms in publications **IV**, **VI**, and **VII**. This potential has been developed explicitly to describe the energetics of collisions of nuclei screened by electrons. The potential is based on a universal

screening function fitted to theoretically obtained potentials for a large set of atom pairs. The screening function is used to model the modification by the electron clouds of the colliding atoms to the naked Coulombic repulsion of the nuclei.

In molecules and crystal structures with covalent bonding the bonds tend to have strongly preferred directions of the bonds, and this is the case in the bonding configurations of carbon and boron nitride (see Fig. 1). Such structures cannot be described using pair potentials, as pair potentials are oblivious to directions of the neighbouring bonds by definition. To address this issue, more complex potential formulations have been developed.

Tersoff-type bond order potentials [138, 139] are one example of such formulations. In publications **IV** and **VII** the carbon-carbon interactions were modelled using the second-generation reactive empirical bond-order Brenner potential [140], and in publication **VI** the boron-nitrogen interaction was modelled using the Albe-Möller many-body potential [141, 142], both of which are of Tersoff-type.

In the Tersoff formalism the total energy of the system is given as a sum over individual atoms as

$$E = \sum_i E_i = \frac{1}{2} \sum_{i,j \neq i} V_{ij}, \tag{3}$$

where

$$V_{ij} = f_c(r_{ij})[Ae^{-\lambda_1 r_{ij}} - B_{ij}e^{-\lambda_2 r_{ij}}]. \tag{4}$$

Here f_c is a cutoff function, which limits the distance beyond which interactions of atoms is not considered and goes smoothly to zero after a predefined cutoff distance. A, λ_1 and λ_2 are fitted constants. All deviations from a simple pair potential are incorporated in B_{ij}, the bond order parameter, which accounts for the effects of number of neighbouring atoms and the relative directions of the bonds:

$$B_{ij} = B_0 e^{-z_{ij}/b} \tag{5}$$

$$z_{ij} = \sum_{k \neq i,j} [w(r_{ik})/w(r_{ij})]^n \times [c + e^{-d\cos\theta_{ijk}}]^{-1} \tag{6}$$

$$w(r) = f_c(r)e^{-\lambda_2 r} \tag{7}$$

The first term in equation 6 determines how much the closer neighbours are favoured over more distant ones and the latter term controls the dependence on the bond angle (θ_{ijl} is the angle between the bonds, B_0, b, n, c and d are constant parameters).

Additional issues to consider in MD simulations are, *e.g.*, how should the atoms at the borders of the simulated system behave, how should interactions with the surrounding world be treated in terms of heat exchange and pressure, and in how small steps should the numerical integration of the equations of motion proceed.

All of the AP MD simulations presented in the publications were run using the PARCAS code [143]. In this code the simulation time step is not fixed, but is varied based on the fastest moving particles in the system, so that no particle is allowed to jump to unrealistic positions (which can result from too coarse time sampling) but on the other hand computational efficiency is maintained as the time step can be kept rather long in the case of only slowly moving particles. The atoms at the edges of the system are connected to a heat bath using the Berendsen thermostat [144] in order to suppress acoustic waves originating from the ion impact site and to prevent their reflection from the system edges. However, it was observed that the parameterization of the thermostat did not strongly affect the simulation results.

5.1.2 Density functional theory

As mentioned earlier, density functional theory (DFT) can be used to make a much more accurate and detailed description of interactions of the nuclei and electrons in matter. As this approach is used in some of the publications within this thesis, it is briefly discussed here. However, many details are omitted as the method was employed by a colleague and not by the author of this thesis. A detailed description of the DFT approach can be found, *e.g.*, in Ref. [145].

DFT is a quantum mechanical method, which is based on the Hohenberg-Kohn theorems [146], which state that an electron density spanning over the 3 spatial coordinates can uniquely determine the ground-state properties of a many-body system comprising of N interacting electrons in an external potential. This potential is defined by the locations of the nuclei in the system, which implies the Born-Oppenheimer approximation. Second, a universal functional for the system energy in terms of the electron density can be derived, and the exact ground state energy of the system is the global minimum value of this functional. Further on, the electron density which minimizes the functional is the exact ground state electron density. The advantage of dealing with the electron density, rather than individual electrons, is that the many-body problem of N electrons with 3N spatial coordinates is reduced to 3 spatial coordinates.

In practice, further approximations are often employed, such as replacing the exact description of the atom's core electrons with so called pseudopotentials, as these electrons do not directly participate in bonding in molecules as well as abstracting the electron-electron interactions in order to achieve gains in computational efficiency. In the widely employed Kohn-Sham ansatz, the problem of many interacting particles is reduced to a problem of non-interacting particles in an Kohn-Sham potential [147]. The exchange and correlation interactions of the particles are described by an exchange-correlation functional included in the potential in which the non-interacting particles move.

5.2 Monte Carlo

Monte Carlo (MC) is a hypernym incorporating many different computational methods. The most important and perhaps only common denominator is the use of random numbers in the methods, from which the name Monte Carlo stems as well, pointing to the famous casino in Monaco. The two MC approaches used within the studies presented in this thesis are random sampling (this can be thought of as Monte Carlo integration) and the kinetic Monte Carlo algorithm.

5.2.1 Transport of Ions in Matter

A computer code named Transport of Ions in Matter (TRIM) [148] has become an ubiquitous tool for predicting the effects of energetic ion bombardment in materials. It is a MC approach in the sense that in order to gather statistics and find average effects of continuous irradiation, a large number random impact events are simulated. Additionally the target structure is described statistically so that the incoming ion has a given probability of hitting a target atom, with the probability depending on the atomic density of the target. Binary collisions between the ion and the atoms are simulated using the Ziegler-Biersak-Littmark universal repulsive potential [137]. The ion trajectory is followed until the ion comes to rest.

The created damage can be estimated in two ways. Either displacements of atoms are explicitly considered so that if in an collision an atom is given more energy than a displacement threshold energy given as an input parameter, the atom is displaced from its location and its path is tracked in the target medium in the same way as that of the primary ion. This leads to collisional cascades progressing in the material, and the total number of displacements is considered to be the amount of damage produced in the target. In reality, during prolonged irradiation some

displaced atoms can recombine with vacancies, and the the total amount of accumulated defects is likely to be lower than the number of displacements.

However, the detailed calculation of the collision cascades is somewhat expensive computationally, and the effects of the cascades can be approximated using the Kinchin-Pease model [149–151] in which the energy transferred in a primary collision of the ion and a target atom is scaled to account for electronic losses and this energy is used to estimate the number of displacements by, roughly speaking, dividing the scaled transferred energy by the energy required to produce one displacement.

An informative quantity named displacements per atom (dpa) can be derived from the damage creation statistics produced by TRIM. Once the average number of displacements produced by a single ion impact is known, the total number of times each atom on average has been displaced after a given irradiation dose can be estimated. This quantity can be used to quantify the level of atomic disorder induced by a given irradiation treatment.

The TRIM approach can produce reliable statistical estimates on the damage production in bulk targets, where the detailed atomic structure is 'averaged out', but as is shown in publication **IV**, the used approximations fail, when the target is shrunk down to nanoscale, with atomically thin graphene and white graphene being the extreme cases.

5.2.2 Kinetic Monte Carlo

Kinetic Monte Carlo (kMC, sometimes referred to as dynamical Monte Carlo) [152] is most commonly used to model thermally activated processes where the rates of the processes can be derived based on the system temperature and heights of the energy barriers for the processes. However, the method can be used to model any process if certain conditions are met.

One important thing to understand about kMC is that the rates at which the processes are taking place are not generated by the method, but are needed as input parameters. For example in the case of the irradiation simulations presented in publications **V** and **VII**, the event rate is deduced from the irradiation intensity (frequency of an ion/electron hitting the target) and from the probabilities of creating each kind of damage on impact, derived from DFT or MD calculations.

The modelled processes have to be Poisson processes, meaning that the events must be independent of each other and occur with non-discrete time intervals. This criterion is met when ion/electron impacts are studied. As a simple case, uniform irradiation of a surface can be

considered: The particles hit the surface at random locations and at random times. The point of one impact does not affect the point of the next one nor are the timings of the impacts correlated.

If the rates are correct and the Poisson process criterion is met, the kMC method does model the time evolution of a system correctly. The mechanisms behind the processes are abstracted away, leading again to great gains in computational efficiency. In the case of the irradiation simulations, the time evolution of the targets under continuous irradiation can be modelled, which would be out of the reach of the more detailed methods described above.

6 Ion irradiation induced damage in multi-walled nanotubes

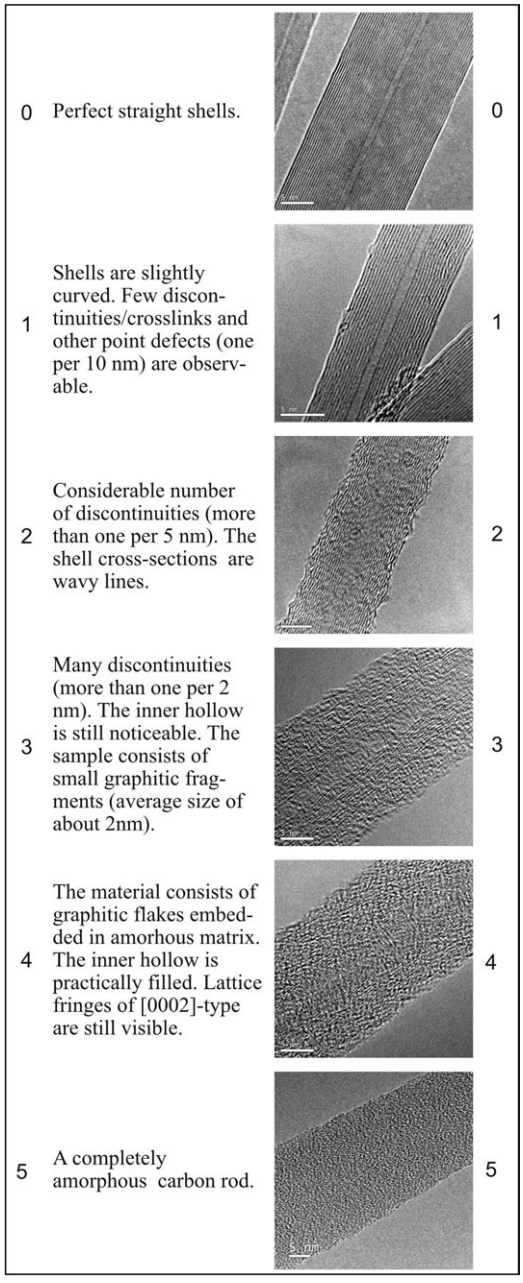

Figure 12: A universal damage scale for quantifying damage in nanotubes, based on transmission electron microscope images. Reproduced from publication **III**.

The common theme of the three experimental publications **I**, **II**, and **III** is characterization of carbon and boron-nitride nanotubes after various ion irradiation treatments. The main characterization tool in these studies is TEM. Raman spectroscopy is also employed, but as is shown in publication **III**, Raman spectroscopy has inherent limitations, which prevent quantification of the non-uniformly distributed damage produced by ion irradiation.

6.1 Universal damage grade

In publication **III** a universal damage grade is presented. As results from the irradiation experiments started to accumulate, it quickly became evident, that drawing any conclusions on the effects of the many differently parameterized irradiations by simply comparing the TEM images to each other gets close to impossible without a common point of reference.

This is obviously an ages old problem to which common units of measurement have been brought in as a solution. If a universal numerical value can be assigned on a property being investigated, comparison of different samples gets straightforward and one does not need to compare a new sample to all the old ones to establish its relative condition, as the numerical value pinpoints the position of the new sample in the big picture.

The universal damage grade was constructed to address this issue when assessing the level of damage in multi-walled nanotubes, and it is show in Fig. 6. In the scale, a value of 0 stands for a perfect defect free nanotube and a value of 5 for a completely amorphous nanorod. This scale is readily employed in publication **III** and can be used to quantify the level of damage in the specimens presented in the earlier publications **I** and **II** in order to gain a broader perspective on the ion irradiation response of the materials investigated.

6.2 Multiwalled carbon nanotubes

In publications **I** and **III** MWCNTs were irradiated with ions and characterized afterwards using TEM and Raman spectroscopy. In publication **I** specific attention was given to cobalt nanorods encapsulated in the open hollow of MWCNTs (such rods can originate from a cobalt catalyst used in the nanotube synthesis) which will be discussed shortly.

The roles of the ion species, ion energy, irradiation fluence and target temperature were mapped. In the case 40 keV Ar^+ ions, the irradiation fluence, which leads to complete amorphization, was determined to be 5.5×10^{15} ions/cm^2 (after a fluence of 1.1×10^{15} ions/cm^2 some organized structure could still be observed). MWCNTs were observed to be more resilient under 350 keV He^+ ion irradiation, in the sense that approximately two orders of magnitude higher fluence produced comparable damage as compared to 40 keV Ar^+ irradiation, whereas 30 keV C irradiation required approximately twice the fluence of 40 keV Ar^+ to produce similar level of damage.

MWCNTs have been observed to preserve their structure under electron irradiation at elevated temperatures due to vacancy [153] and to some extent adatom/interstitial migration [154, 155] (so called *in situ* annealing). As the origin of the damage should not affect the migration of the defects, similar effects could take place under ion irradiation. However, electron irradiation typically creates only point defects (single displaced carbon atoms), but ion irradiation can produce more and larger defects by a single impact and it is not clear *per se*, whether such defects can be annealed *in situ*.

The results of publication **I**, where MWCNTs showed damage after ion irradiation even at an elevated temperature seemed to indicate that high temperature does not protect the tubes under ion irradiation. However, in publication **III** the effects of target temperature were probed more systematically. After the amorphizing fluence of 5.5×10^{15} ions/cm^2 for 40 keV Ar^+ ions was established, a set of samples were irradiated using the same irradiation parameterization, but by gradually increasing the target temperature from sample to sample. Clear improvement in

the irradiation resilience of MWCNTs was observed, once the sample temperature was elevated to 300°C and above (similar behaviour was observed when using 30 keV C^+ ions). These results show that *in situ* annealing *does* take place also under ion irradiation, but the damage is not healed as completely, as under electron irradiation, where the cylindrical shape of the tube walls can be preserved even under prolonged irradiation at elevated temperatures.

Another investigated issue was the role of the energy transfer mechanism in creation of damage in MWCNTs. The loss of kinetic energy of an ion moving in matter is often divided into two categories [137]. The first is commonly called nuclear stopping and is related to elastic collisions between the ion and the target nuclei screened by electrons. The second is termed electronic stopping and stems from inelastic collisions between the ion and target electrons, which are excited from their ground states by the ion.

Graphite has been shown to be quite resistant to energy deposited through electronic stopping in terms of damage created. In both experimental [156] and theoretical [157] works on highly oriented pyrolitic graphite it has been established that if the energy deposited by an energetic ion is less than 7 keV/nm, no damage is inflicted (this does not rule out displacements through elastic collisions), which is attributed to the high thermal and electrical conductivity of the graphene layers. Hence, below the 7 keV/nm threshold irradiation damage should be governed by the elastic collision events.

With none of the parameterizations used in publications **I** and **III** the electronic stopping power exceeds 1 keV/nm. However, the level of damage observed in the samples is much higher than what can be expected from nuclear stopping only, especially in the case of 1.4×10^{17} ions/cm^2 fluence of 350 keV He^+ ions. This is all the more striking since damage rates based on nuclear stopping are known to be overestimated at nanoscale targets [28], essentially due to the fact that a large portion of the displaced atoms escape the system before using all of their kinetic energy for further damage creation.

Consequently, MWCNTs appear to be more susceptible to damage through electronic stopping than bulk graphite. This can be understood by the quasi-one-dimensional structure of the nanotubes: In graphite, the deposited energy can dissipate in the two dimensions of the graphene sheets, whereas in a nanotube the dissipation channels are essentially limited to one dimension. Correlations between electronic and nuclear stopping in nanoscale system can also give rise to enhancement in damage production [28, 158].

6.3 Multiwalled boron nitride nanotubes

In publication **II** the response of BNNTs to ion irradiation was investigated. Irradiation using 40 keV Ar^+ ions and 350 keV He^+ ions was conducted, which enables comparison to the results for MWCNTs reported in publication **III**. In the case of 40 keV Ar^+ ions, a fluence of 2×10^{15} ions/cm^2 was found to be enough to amorphize a multi-walled BNNT (it could be argued that the amorphized BNNT in publication **II** has a damage grade of 4 instead of 5), which is slightly less than the fluence found to amorphize a MWCNT but higher than the next highest fluence investigated (with MWCNTs). Here, the ion-irradiation-response seems to be quite similar with the two types of nanotubes. With the used ion-energy combination, nuclear stopping is the dominant mechanism of energy transfer. Since the atomic masses and bond strengths of the two target materials are similar, such a behaviour can be expected. The results of publications **IV**, **VI** and **VII** give further support to this, as will be discussed later on.

In the case of 350 keV He^+ ions, where electronic stopping is the dominant energy loss mechanism, the situation is quite different. After an irradiation fluence of 3.5×10^{16} ions/cm^2 a BNNT shows very little damage and even after a fluence of 1.2×10^{18} ions/cm^2 the sample is far from amorphized (in this case the high intensity beam might have heated the tube significantly). This behaviour is different from what was observed in the case of MWCNTs, which became badly damaged after comparable irradiation fluences.

If the hypothesis regarding the importance of electronic stopping as a source of damage in MWCNTs is assumed to hold, the results on BNNTs would seem to indicate much lower susceptibility with this material (electronic stopping with 350 keV He ions is almost identical with the two materials, calculated as described in [137]). This behaviour is backwards from what is normally observed with metals and insulators: Insulators are typically much more easily damaged through electronic stopping than metals. Establishing the reason for this would require further investigations, and here it is possible to only speculate, but one reason for the discrepancy could lie in the way the electronic stopping power is estimated in the framework of Ref. [137]: No distinction is made based on the actual electronic structure of the target material, but rather averaged results are used. On the other hand it is known that electronic stopping power can be lower in targets with a wide band-gap (like BNNTs), since the energy transfer to the target electrons is attenuated, due to the requirement of minimum energy transfer to overcome the band-gap [137]. Still, a wide band-gap does not inevitably lead to lower electronic stopping as shown, *e.g.*, in Ref. [159].

The effects of target temperature during irradiation was studied in publication **II**. Strong evidence of the *in situ* annealing effect taking place in BNNTs was found at a temperature of 900 K. Although boron vacancies can be mobile at this temperature, they coalesce with other vacancies once they meet them, and other types of vacancies should not be even close to mobile at 900 K [160]. Thus, vacancy migration, which is important for the *in situ* annealing effect in the case of MWCNTs, should not take place in BNNTs. Although interstitials can be expected to be mobile at room temperature in *h*-BN, they could play a larger role in the *in situ* annealing in BNNTs than in MWCNTs.

6.4 Encapsulated cobalt nanoclusters

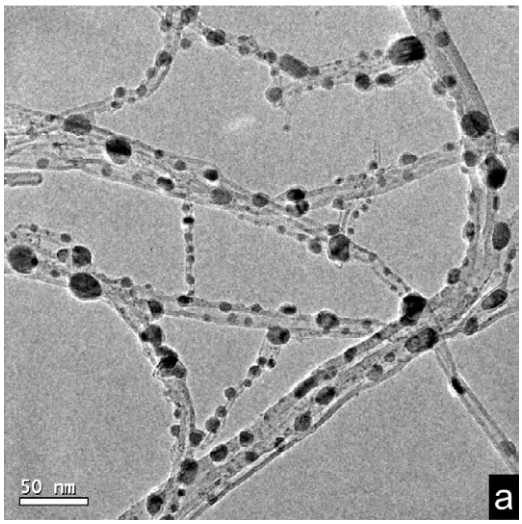

Figure 13: Cobalt nanoclusters on and embedded in MWCNTs after ion irradiation at an elevated temperature.

The nanotubes investigated in publication **I** had the hollow inside the tubes partly filled with cobalt metal, which had served as a catalyst in the nanotube synthesis. Earlier studies had shown that MWCNTs shrank in diameter when irradiated with electrons at elevated temperatures, and consequently extreme pressure was exerted on metals encapsulated in the tube [161]. This was attributed mainly to the sputtering of carbon atoms and subsequent reconstructions of the hexagonal network, which gradually decreases the diameters of the MWCNT shells [162]. Similar behaviour was reported after irradiation with 100 MeV Au ions [163].

Irradiation with $40 - 380$ keV C^+ and He^+ ions at elevated temperatures induced quite different behaviour as shown in publication **I**: No shrinkage of the MWCNTs was observed and the tubes became damaged. The most striking difference to the electron irradiation experiments was observed in the cobalt inside the tubes as the nanorods were transformed in to more or less spherical clusters both on top of the damaged tubes as well as embedded inside the walls (see Fig. 13).

The inverse Ostwald ripening effect [164] can explain this behaviour. Nanoclusters tend to agglomerate at high temperatures and form larger clusters thus lowering the surface to volume ratio of the clusters. Ion irradiation, however, causes mixing in the target, driving the system

towards a more uniform distribution of impurities, as atoms are displaced out of the clusters. These two competing mechanisms can lead to a quasi-equilibrium size of the clusters, similar to what was observed in publication **I**.

6.5 Raman spectroscopy with non-isotropic targets

Raman spectra were measured from all the irradiated samples in publications **I**, **II** and **III**. In general the spectra show similar behaviour to what is observed in the TEM images: The D-band becomes more intense and the peaks become wider with increasing irradiation fluence. Quantification of the level of damage is not straightforward though, as is discussed at length in publication **III**.

The problem is related to the spatial distribution of damage induced by ion irradiation, which is in practice never uniform. Conventional Raman spectrum on the other hand represents essentially a weighted average of signals originating from many depths in a sample. Due to absorption of light traversing matter, the measured signal at a given wavelength can be written as

$$I_R(\lambda) = I_0 \int_0^t i_R(\lambda, z) e^{\frac{-2z}{\alpha}} dz, \qquad (8)$$

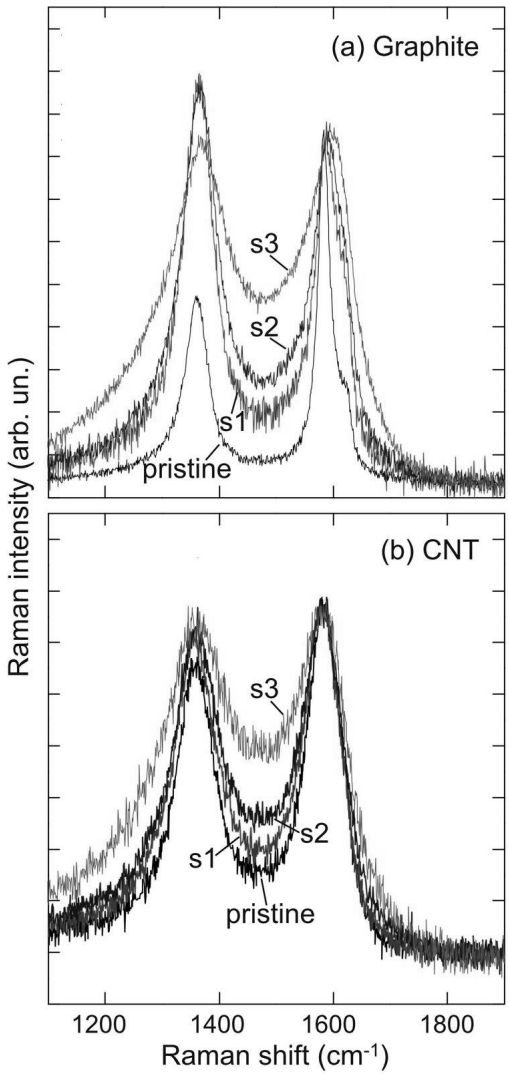

Figure 14: Raman spectra from three samples with the same total number of defects, but with different spatial distributions (from publication **III**).

where $I_R(\lambda)$ is the total measured signal intensity at wavelength λ, I_0 is the initial laser intensity, t is the sample thickness, $i_R(\lambda, z)$ is the partial Raman signal intensity originating from depth z and $e^{\frac{-2z}{\alpha}}$ is the attenuation factor, where α is the absorption coefficient (assuming no dependence of α on λ, which is not necessarily always the case [165]).

The definite integral in Equation 8 disposes of all spatial information related to the depth coordinate z. Also, it is easy to imagine many different variations of $i_R(\lambda, z)$, which would produce the same resulting $I_R(\lambda, z)$. Further on, the sample thickness t affects the total measured signal, especially if the sample is so thin that the attenuation factor is still $\gg 0$ at the bottom of the sample.

All this adds up to inherent ambiguity of Raman spectra measured from non-isotropic samples. This effect can be observed in publication **II**, where the Raman spectra measured from the samples even after the highest fluences, which according to TEM amorphized the surface almost completely, indicate only limited amount of damage: Most of the signal originates from deeper parts of the sample, outside of the range of the ions.

More systematic exploration of this issue was conducted in publication **III**, where three graphitic and MWCNT samples were irradiated using different ion energies, but fluences chosen in such a way that similar total amount of defects was produced, but with different spatial distributions. The Raman spectra measured from those samples were indeed quite different (see Fig. 14), with the sample with damage most concentrated near the surface seeming to be the most damaged. Without *a priori* knowledge of the defect distributions, it would be impossible to deduce that the three samples actually have approximately the same total amount of defects.

7 Irradiation induced damage in hexagonal monolayers

As was mentioned earlier, 'traditional' estimates on defect production through irradiation can fail when the target is shrunk to nanoscale. One central reason for this is the assumption that the energy deposited into the target via the incoming particles is (almost) completely absorbed by the target. This energy is further assumed to be used for displacing atoms through collisions, generation of phonons, and electronic excitations. However, in nanoscale targets (atomically thin graphene and white graphene being the ultimate examples), typically large part of the kinetic energy of the incoming particle, as well as recoiled target atoms is 'lost' as they escape the system before having a chance to use the energy for further damage production. In publications **IV**, **V**, **VI**, and **VII** the issue of damage production in hexagonal monolayers is addressed.

7.1 Electron irradiation of white graphene

The simplest approximation in estimating damage created by energetic particles, is the binary collision approximation, where the incoming particle is assumed to interact with a single target atom at a time and the probability of ejecting this atom from the system is estimated. It is further assumed, that the incoming particle and, in the case of a displacement, the displaced target atom escape the system.

In the case of electron irradiation of an atomically thin monolayer in direction normal to the target, within the energy ranges of modern transmission electron microscopes (<300 keV), the binary collision approximation is valid: In order to transfer enough energy to a target atom to displace it, the electron trajectory has to go so close to the atom that this can happen with only one atom at a time. Further on, due to conservation of energy and momentum, the maximum angle at which a B atom can be scattered by an electron within the used energy ranges is approximately 60° (calculated as described in [154]), meaning that the recoiled atom will not hit the surrounding atoms.

Within the binary collision approximation, the threshold energy for a displacement (T_d) is what governs the predictions of the model. T_d is the minimum amount of kinetic energy that an atom must be given for it to be able to break its bonds with the surrounding atoms and escape the system (very much akin to the escape velocity of a rocket from the gravitation field of a planet).

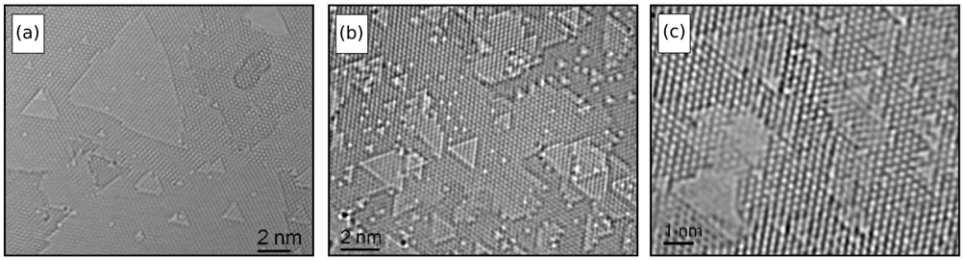

Figure 15: Triangular holes in white graphene observed under electron irradiation with energies of (a) 80 keV, (b) 120 keV, and (c) 200 keV. Reproduced from publication **V**.

In publication **V**, DFT was applied to calculate the T_d values for both B and N atoms in white graphene. The motivation for these calculations was the peculiar shapes of the vacancies observed under electron irradiation: The vacancies were consistently of triangular shape oriented in the same direction (see Fig. 15) with nitrogen terminated edges [6]. Asymmetry in the T_d values for B and N would explain the observed shape, but earlier calculations [166] had the $T_d^B > T_d^N$. Due to the lower mass of boron, its is more probable to displace a boron atom than

nitrogen as calculated based on the threshold values reported in Ref. [166], but the probabilities are so close to each other that they cannot explain the strong asymmetry observed in experiments. However, those calculations were based on the tight binding approximation, which does not take the significant charge transfer [35] in the 'ionic' *h*-BN into account and, in fact, the more sophisticated DFT calculations reported in publication **V** had the relationship of the T_d values reversed.

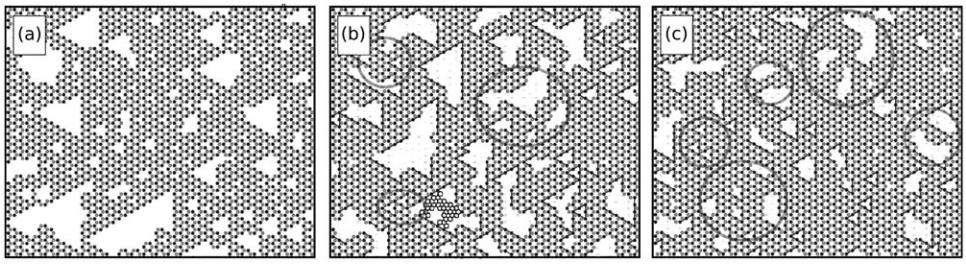

Figure 16: Results of the kMC simulations of white graphene under electron irradiation with an energy of (a) 80 keV, (b) 120 keV, and (c) 200 keV. Nitrogen terminated edges are marked with lines in panels (b) and (c). Reproduced from publication **V**.

A kMC model was developed based on the binary collision approximation, the new calculated T_d values, and the McKinley-Fesbach formalism for Coulombic scattering of relativistic electrons [154,167]. Example results of the simulations are shown in Fig. 16. Especially in the case of the lower electron energies, the simulated structures and experimental images match well, with similar triangular holes appearing in both cases. In the highest energy case (200 keV) the triangular shape is not reproduced as well, but still N atoms are the typical edge atoms with approximately 2:1 ratio to B.

Altogether, the asymmetric threshold energies seem to explain the shape of the holes seen in the experiments. At the highest energy the triangles are more regular in the experiments, however, which could indicate that some other process is contributing as well, such as adatom migration, or chemical etching due to non-perfect vacuum level.

7.2 Ion irradiation of graphene and white graphene

In the case of ion irradiation of atomically thin monolayers it is not as clear as with electron irradiation whether the binary collision approximation can be applied. Hence, in publication **IV** the predictions on defect production obtained with different methods are compared. Production of damage in graphene is modelled using the binary collision approximation, the computer program TRIM, and AP MD. Although the sputtering rate could be estimated up to a certain

accuracy (as compared to the AP MD results) with the binary collision approximation, the TRIM results agreed poorly with the MD results. Also the binary collision approximation disagreed with the MD results, especially where the sputtering rate exceeded 1, which can be expected already from the fact that the assumption of a binary collision of the ion and only one target atom does not hold when many atoms are sputtered at a time.

More fundamental problem with both the binary collision approximation as well as the TRIM approach is that they do not take the atomic structure of the target into account. In the case of the binary collision approximation, collision cascades are never taken into account, although recoiled atoms can in fact hit the neighbouring atoms (with a fast moving ion, momentum transfer can occur very close to a perpendicular direction relative to the trajectory of the ion). In the case of TRIM, collision cascades happen too often, as the target is assumed to be a homogeneous slab of set thickness rather than an atomically thin membrane. Further on, information on the features of the produced defect structures can not be acquired using these two methods.

For these reasons, a large number AP MD simulations of ion impacts were conducted on both graphene and white graphene. In publication **IV**, impacts of He, Ne, Ar, Kr, and Xe ions, with kinetic energies ranging from 35 eV to 2 MeV on graphene in the normal direction of the target plane, were simulated, and statistics on sputtering rates, and types and abundances of defects were gathered. In publication **VII** the parameter space was expanded to cover arbitrary angles of incidence up to 88° (see Fig. 17). In publication **VI** similar simulations were conducted on a white graphene target. Approximately 4 million simulations were conducted in total.

The probabilities of creating the different types of defects in graphene and *h*-BN presented in publications **VI** and **VII** are qualitatively very similar. With both of the targets a peak in single vacancy production is found at low ion energies $\lesssim$1 keV with normal angle of incidence, with the precise location depending on the ion species. The peak moves towards higher energies when the ion beam is tilted relative to the sample surface. Similar behaviour can be observed in the case of double vacancies and complex vacancies (the maxima of complex vacancy production probabilities are first shifted towards lower energies, when the beam is only slightly tilted). Further on, the different types of defects find their production probability maxima at different locations in the ion-energy–angle-of-incidence parameter space, which means that selectivity in terms of produced types of defects can be achieved. Additionally, as focused ion beam systems operate often at a fixed voltage (typically 30 kV), the tilting of the target can be used to control the types of defects produced, as is demonstrated in publication **VII**.

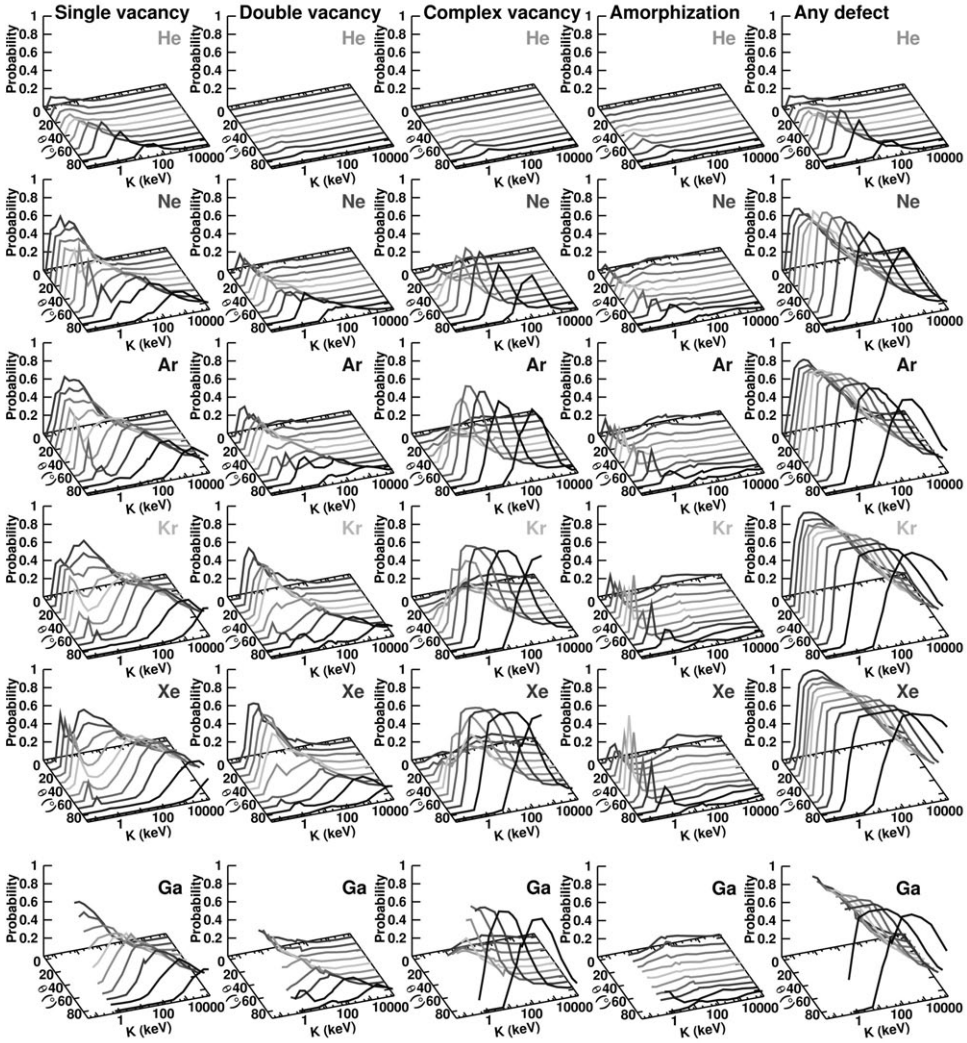

Figure 17: Probabilities of producing various types of defects (see Fig. 8 for example structures) in graphene under an impact of an energetic ion. Reproduced from publication **VII**.

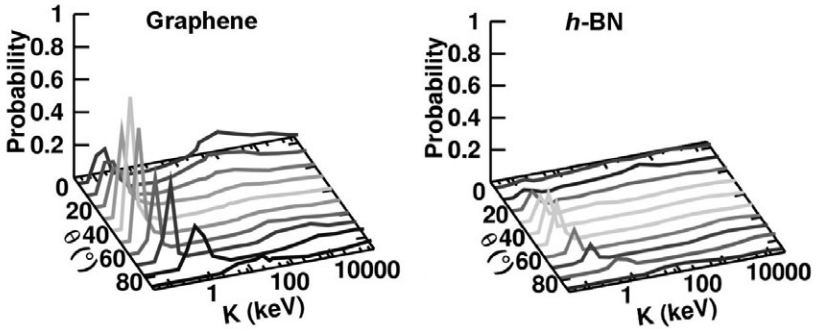

Figure 18: Probabilities of creating an amorphization by an impact of a Xe ion in graphene and white graphene.

As stated above, the response of graphene and white graphene to ion irradiation is very similar. This indicates that the chemistry and the type of bonding is not an important factor in the damage production. Rather, the damage production is governed by the geometry of the target, and the ballistic collisions of the ion and the recoiled atoms. One exception to this can be observed, and that is the case of amorphizations. The probabilities of producing an amorphization with Xe ions in graphene and white graphene is compared in Fig. 18. Creation of an amorphization in graphene is distinctively more probable than in white graphene. This can be explained by the binary nature of boron nitride. In a typical amorphization event an atom is first displaced in the in-plane direction of the sheet after which it is bonded to the neighbouring atoms, possibly causing further reorganization of the surrounding atoms. In a unary carbon system a locally stable configuration can be more easily achieved than in binary *h*-BN, again due to the unfavoured B-B and N-N bonds, and hence the recoiled B and N atoms are more likely to simply escape the system leading to a vacancy type defect.

In order to assess the reliability of the analytical potentials used in the AP MD simulations, DFT calculations were conducted. The displacement thresholds agreed well when calculated using the two methods. This, combined with the accurately reproduced energetics of defects by the used potentials [140,168], shows that the results of the AP MD simulations are reliable. The reason for not using the more accurate DFT approach directly for all the impact simulations is the vast number of simulations required for probing the whole parameter space considered, which makes such a task impossible.

Handling and presentation of the increasingly large amount of data produced by the simulations gets quickly problematic. General trends in defect production can be observed in plots such as in Fig. 17, but precise numerical values are difficult to extract. Additionally, the number of sputtered atoms and sizes of produced defects are not typically Gaussian distributed, which means that mean values and standard deviations can not be used to describe the observables either. For this reason a kMC code was developed and made publicly available through a web browser based interface [169]. The kMC simulation takes as its input defect creation probabilities, in terms of number of sputtered atoms and size of the defect, from the AP MD simulations. Using the kMC code, simulation of a graphene sheet under ion irradiation with a specified parameterization at macroscopic timescales can be performed. Example output of the code is shown in Fig. 19.

It should be pointed out that as in the case of any theoretical predictions, experiments need to be conducted to ascertain the correctness of the calculations. One specific concern is the role of electronic stopping. Since experiments indicate that electronic stopping should not lead to damage in the considered targets [156,157,170,171], electronic excitation effects were not taken

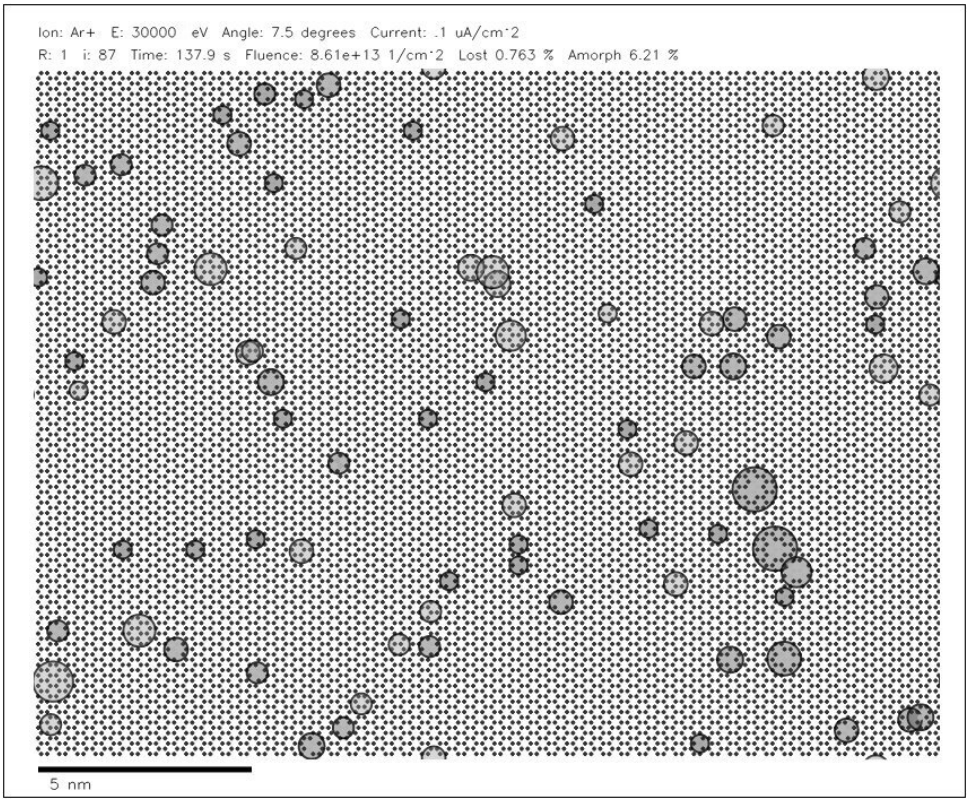

Figure 19: An example result of the kMC simulation code modelling ion irradiation of graphene. The dots mark carbon atoms and missing dots represent sputtered atoms. The circles represent the affected area of each impact, meaning area where the perfect hexagonal structure of graphene is altered.

into account in the simulations. However, the results of publication **III** suggest, that electronic excitations could have stronger effects in nanoscale materials, and hence this issue needs to be addressed in the future. The effect is not necessarily as strong in the monolayer targets, as there the excitations can dissipate in two dimensions in contrast to the one dimensionality of the nanotubes investigated in publication **III**.

8 Conclusions

In this thesis seven articles published (6) or under review (1) in international peer-reviewed journals were presented along with this introduction, where the backgrounds of the studied materials and employed methods were reviewed, and the findings reported in the publications summarized.

The presented research focused on irradiation-induced structural changes in graphene, carbon and boron nitride nanotubes, and hexagonal boron nitride monolayer (a.k.a. white graphene). Throughout the summary, special attention was given to the similarities and differences of the monatomic carbon and binary boron nitride structures. Multi-walled nanotubes under ion irradiation were investigated using transmission electron microscopy and Raman spectroscopy as the tools for characterization of the irradiation-induced effects. A universal damage grade based on transmission electron microscopy images was presented for quantifying the level of damage in a multi-walled nanotube after an irradiation treatment. The shortcomings of Raman spectroscopy in characterization of irradiation-induced damage, related to non-uniform distribution of the defects, were discussed. The response of the two types of nanotubes was studied to specific types of irradiation (*e.g.*, 40 keV Ar^+ and 350 keV He^+). An elevated temperature was discovered to protect both types of nanotubes from damage accumulation, which was attributed to enhanced mobility of point defects. Cobalt nanorods encapsulated inside the hollow of a multi-walled carbon nanotube were observed to transform into roughly spherical nanoparticles on top and embedded in the nanotube walls during ion irradiation at an elevated temperature.

Multi-scale atomistic simulations were carried out in order to model the response of graphene and white graphene to irradiation. White graphene under electron irradiation was studied using first-principles molecular dynamics and the kinetic Monte Carlo method. The peculiar triangular shape of vacancies observed under transmission electron microscope was explained based on asymmetry of the displacement threshold energies for boron and nitrogen atoms.

Comprehensive statistics on defect production in graphene and white graphene under ion irradiation, in terms of types and abundances of produced defects, were generated using analytical potential molecular dynamics simulations. The roles of the ion species, ion energy, and the angle of incidence of the ion were studied in detail. Based on the molecular dynamics simulation results, a kinetic Monte Carlo model was developed and made publicly available, which can be used for simulating the evolution of the target material under continuous irradiation at macroscopic timescales.

Altogether, the results presented in the seven publications in this thesis shed new light on the effects of energetic particle bombardment on the studied materials. This information can be of high value when the materials are to be employed in applications. If the materials are to be used in radiation hostile environments, it is of great importance to understand how quickly they will deteriorate to correctly asses the life-time of the structures. On the other hand, many of the properties of the studied materials can be tailored by controllably modifying the atomic structure of the materials, and the results presented in this thesis can be useful when planning such modifications.

Although the results presented in this thesis provide a consistent picture of the response of graphene and BN sheets to irradiation, the theory of irradiation effects in 2D materials is far from being complete. With regard to planar systems, the theoretical predictions on defect production in graphene and white graphene need to be experimentally verified, *e.g.*, by combining ion irradiation with transmission electron microscopy. The role of electronic stopping in defect production in nanoscale materials must be studied in a more detailed fashion, where both experimental and theoretical methods can be employed. Also, graphene is often supported on top of a bulk substrate in experiments, and the effects of the substrate on defect production under ion irradiation requires further studies. Finally, one of the key issues is the generalization of the results to other 2D materials, including transition metal dichalcogenides and oxides sheets, which have recently been manufactured [172, 173].

ACKNOWLEDGEMENTS

I wish to thank the head of the Department of Physics at the University of Helsinki, Professor Juhani Keinonen, and the head of the Division of Materials Physics, Professor Jyrki Räisänen, for providing the facilities for my research presented in this thesis. I would also like to thank Professor Juhani Keinonen for supervising my work during the preparation of the thesis, while allowing me much freedom for independent explorations.

I am infinitely indebted to Docent Arkady Krasheninnikov for looking after me during the whole duration of my PhD studies. Special credit should be given for the fact, that while being a theorist, he kept on pushing me forward on the (often frustrating) experimental front, providing invaluable ideas, contacts and guidance. My thesis would look quite different without the help of Docent Jani Kotakoski. His inexhaustible energy leaks to those around him leaving them flabbergasted with what all can be accomplished within the shortest of times.

A house is as strong as its foundation, and in my case the foundation was built by Docent Eero Rauhala, Docent Tommy Ahlgren and Dr. Kalle Heinola during my pre-graduate studies along with all the other teachers I have had the honor of being a student of throughout my life. Discussions with peers are often most educating and I truly appreciate the smart gang of people whom I've had the privilege of working with, Dr. Antti Tolvanen being my main partner-in-crime during my PhD studies.

The experiments at our laboratory would not happen without the tireless efforts of the technical personnel, headed by Docent Pertti Tikkanen, who knows a thing or two about experimental physics, and I am most thankful for all the help I have received during the years. As is evident from the number of co-authors in all the publications presented in this thesis, I have had an extensive team of superb scientists backing me up, including Professor Florian Banhart, Professor Litao Sun, Professor Dmitri Golberg, Docent Leonid Khriachtchev, and MSc Timur Nikitin to name a few.

Finally, I want to thank my family for everything. The people I have grown up with have very much made me the man I am today, and the process continues. My second family, namely all my dear friends have made their mark as well.

Ja lämpimin kiitos kuuluu rakkaalle vaimolleni Saralle.

Kumpula, May, 2011
Ossi Lehtinen

References

1. K. S. Novoselov, A. K. Geim, S. V. Morozov, D. Jiang, Y. Zhang, S. V. Dubonos, I. V. Grigorieva, and A. A. Firsov, *Electric Field Effect in Atomically Thin Carbon Films*, Science **306**, 666 (2004).

2. L. V. Radushkevich and L. V. M., *O strukture ugleroda, obrazujucegosja pri termiceskom razlozenii okisi ugleroda na zeleznom kontakte*, Zurn. Fisic. Chim. **26**, 88 (1952).

3. A. Oberlin, M. Endo, and T. Koyama, *Filamentous growth of carbon through benzene decomposition*, J. Cryst. Growth **32**, 335 (1976).

4. S. Iijima, *Helical microtubules of graphitic carbon*, Nature **354**, 56 (1991).

5. N. G. Chopra, R. J. Luyken, K. Cherrey, V. H. Crespi, M. L. Cohen, S. G. Louie, and A. Zettl, *Boron Nitride Nanotubes*, Science **269**, 966 (1995).

6. C. Jin, F. Lin, K. Suenaga, and S. Iijima, *Fabrication of a Freestanding Boron Nitride Single Layer and Its Defect Assignments*, Phys. Rev. Lett. **102**, 195505 (2009).

7. J. C. Meyer, A. Chuvilin, G. Algara-Siller, J. Biskupek, and U. Kaiser, *Selective Sputtering and Atomic Resolution Imaging of Atomically Thin Boron Nitride Membranes*, Nano Lett. **9**, 2683 (2009).

8. B. Peng, M. Locascio, P. Zapol, S. Li, S. L. Mielke, G. C. Schatz, and H. D. Espinosa, *Measurements of near-ultimate strength for multiwalled carbon nanotubes and irradiation-induced crosslinking improvements*, Nature Nanotech. **3**, 626 (2008).

9. S. Price, http://science.nasa.gov/science-news/science-at-nasa/2000/ast07sep_1/, last accessed on March 2011.

10. A. Kis, G. Csanyi, J.-P. Salvetat, T.-N. Lee, E. Couteau, A. J. Kulik, W. Benoit, J. Brugger, and L. Forro, *Reinforcement of single-walled carbon nanotube bundles by intertube bridging*, Nat. Mater. **3**, 153 (2004).

11. M.-F. Yu, O. Lourie, M. J. Dyer, K. Moloni, T. F. Kelly, and R. S. Ruoff, *Strength and Breaking Mechanism of Multiwalled Carbon Nanotubes Under Tensile Load*, Science **287**, 637 (2000).

12. M. Sammalkorpi, A. Krasheninnikov, A. Kuronen, K. Nordlund, and K. Kaski, *Mechanical properties of carbon nanotubes with vacancies and related defects*, Phys. Rev. B **70**, 245416 (2004).

13. S. L. Mielke, D. Troya, S. Zhang, J.-L. Li, S. Xiao, R. Car, R. S. Ruoff, G. C. Schatz, and T. Belytschko, *The role of vacancy defects and holes in the fracture of carbon nanotubes*, Chem. Phys. Lett. **390**, 413 (2004).

14. M.-S. Wang, D. Golberg, and Y. Bando, *Tensile Tests on Individual Single-Walled Carbon Nanotubes: Linking Nanotube Strength with Its Defects*, Adv. Mater. **22**, 4071 (2010).

15. J. A. Åström, A. V. Krasheninnikov, and K. Nordlund, *Carbon Nanotube Mats and Fibers with Irradiation-Improved Mechanical Characteristics: A Theoretical Model*, Phys. Rev. Lett. **93**, 215503 (2004).

16. A. H. Castro Neto, F. Guinea, N. M. R. Peres, K. S. Novoselov, and A. K. Geim, *The electronic properties of graphene*, Rev. Mod. Phys. **81**, 109 (2009).

17. D. A. Areshkin, D. Gunlycke, and C. T. White, *Ballistic Transport in Graphene Nanostrips in the Presence of Disorder: Importance of Edge Effects*, Nano Lett. **7**, 204 (2007).

18. L. A. Ponomarenko, F. Schedin, M. I. Katsnelson, R. Yang, E. W. Hill, K. S. Novoselov, and A. K. Geim, *Chaotic Dirac Billiard in Graphene Quantum Dots*, Science **320**, 356 (2008).

19. T. G. Pedersen, C. Flindt, J. Pedersen, N. A. Mortensen, A.-P. Jauho, and K. Pedersen, *Graphene Antidot Lattices: Designed Defects and Spin Qubits*, Phys. Rev. Lett. **100**, 136804 (2008).

20. J. Bai, X. Zhong, S. Jiang, Y. Huang, and X. Duan, *Graphene nanomesh*, Nat. Nano **5**, 190 (2010).

21. E. H. Åhlgren, J. Kotakoski, and A. V. Krasheninnikov, *Atomistic simulations of the implantation of low-energy boron and nitrogen ions into graphene*, Phys. Rev. B **83**, 115424 (2011).

22. M. S. Si and D. S. Xue, *Magnetic properties of vacancies in a graphitic boron nitride sheet by first-principles pseudopotential calculations*, Phys. Rev. B **75**, 193409 (2007).

23. C.-H. Park and S. G. Louie, *Energy Gaps and Stark Effect in Boron Nitride Nanoribbons*, Nano Lett. **8**, 2200 (2008).

24. Z. Zhang and W. Guo, *Energy-gap modulation of BN ribbons by transverse electric fields: First-principles calculations*, Phys. Rev. B **77**, 075403 (2008).

25. V. Tuboltsev and J. Räisänen, *Sculpturing Nanowires with Ion Beams*, Small **5**, 2687 (2009).

26. C. Gomez-Navarro, P. J. D. Pablo, J. Gomez-Herrero, B. Biel, F. J. Garcia-Vidal, A. Rubio, and F. Flores, *Tuning the conductance of single-walled carbon nanotubes by ion irradiation in the Anderson localization regime*, Nat. Mater. **4**, 534 (2005).

27. D.-H. Kim, H.-S. Jang, C.-D. Kim, D.-S. Cho, H.-D. Kang, and H.-R. Lee, *Enhancement of the field emission of carbon nanotubes straightened by application of argon ion irradiation*, Chem. Phys. Lett. **378**, 232 (2003).

28. A. V. Krasheninnikov and K. Nordlund, *Ion and electron irradiation-induced effects in nanostructured materials*, J. Appl. Phys. **107**, 071301 (2010).

29. D. C. Bell, M. C. Lemme, L. A. Stern, J. R. Williams, and C. M. Marcus, *Precision cutting and patterning of graphene with helium ions*, Nanotechnol. **20**, 455301 (2009).

30. M. C. Lemme, D. C. Bell, J. R. Williams, L. A. Stern, B. W. H. Baugher, P. Jarillo-Herrero, and C. M. Marcus, *Etching of Graphene Devices with a Helium Ion Beam*, ACS Nano **3**, 2674 (2009).

31. H. W. Kroto, J. R. Heath, S. C. O'Brien, R. F. Curl, and R. E. Smalley, *C60: Buckminsterfullerene*, Nature **318**, 162 (1985).

32. D. Golberg, Y. Bando, Y. Huang, T. Terao, M. Mitome, C. Tang, and C. Zhi, *Boron Nitride Nanotubes and Nanosheets*, ACS Nano **4**, 2979 (2010).

33. A. Jorio, M. S. Dresselhaus, and G. Dresselhaus, *Carbon Nanotubes: Advanced Topics in the Synthesis, Structure, Properties and Applications* (Springer-Verlag, Berlin, Heidelberg, 2008).

34. M. J. Allen, V. C. Tung, and R. B. Kaner, *Honeycomb Carbon: A Review of Graphene*, Chem. Rev. **110**, 132 (2010).

35. J. C. Meyer, S. Kurasch, H. J. Park, V. Skakalova, D. Künzel, A. Groß, A. Chuvilin, G. Algara-Siller, S. Roth, T. Iwasaki, U. Starke, J. H. Smet, and U. Kaiser, *Experimental analysis of charge redistribution due to chemical bonding by high-resolution transmission electron microscopy*, Nat. Mater. **10**, 209 (2011).

36. N. Ooi, A. Rairkar, L. Lindsley, and J. B. Adams, *Electronic structure and bonding in hexagonal boron nitride*, J. Phys. Condens. Matter **18**, 97 (2006).

37. A. R. Oganov, J. Chen, C. Gatti, Y. Ma, Y. Ma, C. W. Glass, Z. Liu, T. Yu, O. O. Kurakevych, and V. L. Solozhenko, *Ionic high-pressure form of elemental boron*, Nature **457**, 863 (2009).

38. P. R. Wallace, *The Band Theory of Graphite*, Phys. Rev. **71**, 622 (1947).

39. T. Dumitrica, T. Belytschko, and B. I. Yakobson, *Bond-breaking bifurcation states in carbon nanotube fracture*, J. Chem. Phys. **118**, 9485 (2003).

40. C. Lee, X. Wei, J. W. Kysar, and J. Hone, *Measurement of the Elastic Properties and Intrinsic Strength of Monolayer Graphene*, Science **321**, 385 (2008).

41. O. L. Blakslee, D. G. Proctor, E. J. Seldin, G. B. Spence, and T. Weng, *Elastic Constants of Compression-Annealed Pyrolytic Graphite*, J. Appl. Phys. **41**, 3373 (1970).

42. M. Choucair, P. Thordarson, and J. A. Stride, *Gram-scale production of graphene based on solvothermal synthesis and sonication*, Nat. Nanotechnol. **4**, 30 (2009).

43. S. Bae, H. Kim, Y. Lee, X. Xu, J.-S. Park, Y. Zheng, J. J. Balakrishnan, T. Lei, H. R. Kim, Y. I. Song, Y.-J. Kim, K. S. Kim, B. Ozyilmaz, J.-H. Ahn, B. H. Hong, and S. Iijima, *Roll-to-roll production of 30-inch graphene films for transparent electrodes*, Nat. Nanotechnol. **5**, 574 (2010).

44. X. An, T. Simmons, R. Shah, C. Wolfe, K. M. Lewis, M. Washington, S. K. Nayak, S. Talapatra, and S. Kar, *Stable Aqueous Dispersions of Noncovalently Functionalized Graphene from Graphite and their Multifunctional High-Performance Applications*, Nano Lett. **10**, 4295 (2010).

45. R. Saito, G. Dresselhaus, and M. S. Dresselhaus, *Physical Properties of Carbon Nanotubes* (Imperial, London, 1998).

46. S. Reich, J. Maultzsch, C. Thomsen, and P. Ordejón, *Tight-binding description of graphene*, Phys. Rev. B **66**, 035412 (2002).

47. K. S. Novoselov, A. K. Geim, S. V. Morozov, D. Jiang, M. I. Katsnelson, I. V. Grigorieva, S. V. Dubonos, and A. A. Firsov, *Two-dimensional gas of massless Dirac fermions in graphene*, Nature **438**, 197 (2005).

48. Y. Zhang, Y.-W. Tan, H. L. Stormer, and P. Kim, *Experimental observation of the quantum Hall effect and Berry's phase in graphene*, Nature **438**, 201 (2005).

49. R. S. Deacon, K.-C. Chuang, R. J. Nicholas, K. S. Novoselov, and A. K. Geim, *Cyclotron resonance study of the electron and hole velocity in graphene monolayers*, Phys. Rev. B **76**, 081406 (2007).

50. Z. Jiang, E. A. Henriksen, L. C. Tung, Y.-J. Wang, M. E. Schwartz, M. Y. Han, P. Kim, and H. L. Stormer, *Infrared Spectroscopy of Landau Levels of Graphene*, Phys. Rev. Lett. **98**, 197403 (2007).

51. M. Monthioux and V. L. Kuznetsov, *Who should be given the credit for the discovery of carbon nanotubes?*, Carbon **44**, 1621 (2006).

52. M. Hillbert and M. Lange, *The structure of graphite filaments*, Z. Kristallogr. **111**, 24 (1958).

53. J. Abrahamson, P. G. Wiles, and B. L. Rhoades, *Correspondence*, Carbon **37**, 1873 (1999).

54. S. Ogata and Y. Shibutani, *Ideal tensile strength and band gap of single-walled carbon nanotubes*, Phys. Rev. B **68**, 165409 (2003).

55. T. Ozaki, Y. Iwasa, and T. Mitani, *Stiffness of Single-Walled Carbon Nanotubes under Large Strain*, Phys. Rev. Lett. **84**, 1712 (2000).

56. A. Krishnan, E. Dujardin, T. W. Ebbesen, P. N. Yianilos, and M. M. J. Treacy, *Young's modulus of single-walled nanotubes*, Phys. Rev. B **58**, 14013 (1998).

57. X. Wei, Q. Chen, S. Xu, L. Peng, and J. Zuo, *Beam to String Transition of Vibrating Carbon Nanotubes Under Axial Tension*, Adv. Funct. Mater. **19**, 1753 (2009).

58. M. Huhtala, A. V. Krasheninnikov, J. Aittoniemi, S. J. Stuart, K. Nordlund, and K. Kaski, *Improved mechanical load transfer between shells of multiwalled carbon nanotubes*, Phys. Rev. B **70**, 045404 (2004).

59. A. Nagashima, N. Tejima, Y. Gamou, T. Kawai, and C. Oshima, *Electronic Structure of Monolayer Hexagonal Boron Nitride Physisorbed on Metal Surfaces*, Phys. Rev. Lett. **75**, 3918 (1995).

60. A. Nagashima, N. Tejima, Y. Gamou, T. Kawai, and C. Oshima, *Electronic dispersion relations of monolayer hexagonal boron nitride formed on the Ni(111) surface*, Phys. Rev. B **51**, 4606 (1995).

61. E. Rokuta, Y. Hasegawa, K. Suzuki, Y. Gamou, C. Oshima, and A. Nagashima, *Phonon Dispersion of an Epitaxial Monolayer Film of Hexagonal Boron Nitride on Ni(111)*, Phys. Rev. Lett. **79**, 4609 (1997).

62. D. Pacile, J. C. Meyer, C. O. Girit, and A. Zettl, *The two-dimensional phase of boron nitride: Few-atomic-layer sheets and suspended membranes*, Applied Physics Letters **92**, 133107 (2008).

63. Zhu, Y. Bando, L. Yin, and D. Golberg, *Field Nanoemitters: Ultrathin BN Nanosheets Protruding from Si3N4 Nanowires*, Nano Lett. **6**, 2982 (2006).

64. W.-Q. Han, L. Wu, Y. Zhu, K. Watanabe, and T. Taniguchi, *Structure of chemically derived mono- and few-atomic-layer boron nitride sheets*, Appl. Phys. Lett. **93**, 223103 (2008).

65. N. Alem, R. Erni, C. Kisielowski, M. D. Rossell, W. Gannett, and A. Zettl, *Atomically thin hexagonal boron nitride probed by ultrahigh-resolution transmission electron microscopy*, Phys. Rev. B **80**, 155425 (2009).

66. C. Zhi, Y. Bando, C. Tang, H. Kuwahara, and D. Golberg, *Large-Scale Fabrication of Boron Nitride Nanosheets and Their Utilization in Polymeric Composites with Improved Thermal and Mechanical Properties*, Adv. Mater. **21**, 2889 (2009).

67. R. Gao, L. Yin, C. Wang, Y. Qi, N. Lun, L. Zhang, Y.-X. Liu, L. Kang, and X. Wang, *High-Yield Synthesis of Boron Nitride Nanosheets with Strong Ultraviolet Cathodoluminescence Emission*, J. Phys. Chem. C **113**, 15160 (2009).

68. C. Li, Y. Bando, C. Zhi, Y. Huang, and D. Golberg, *Thickness-dependent bending modulus of hexagonal boron nitride nanosheets*, Nanotechnol. **20**, 385707 (2009).

69. J. H. Warner, M. H. Rümmeli, A. Bachmatiuk, and B. Büchner, *Atomic Resolution Imaging and Topography of Boron Nitride Sheets Produced by Chemical Exfoliation*, ACS Nano **4**, 1299 (2010).

70. A. Nag, K. Raidongia, K. P. S. S. Hembram, R. Datta, U. V. Waghmare, and C. N. R. Rao, *Graphene Analogues of BN: Novel Synthesis and Properties*, ACS Nano **4**, 1539 (2010).

71. J. F. Green, T. K. Bolland, and J. W. Bolland, *Theoretical elastic behavior for hexagonal boron nitride*, J. Chem. Phys. **64**, 656 (1976).

72. A. Abdellaoui, A. Bath, B. Bouchikhi, and O. Baehr, *Structure and optical properties of boron nitride thin films prepared by PECVD*, Mater. Sci. Eng., B **47**, 257 (1997).

73. V. L. Solozhenko, A. G. Lazarenko, J. P. Petitet, and A. V. Kanaev, *Bandgap energy of graphite-like hexagonal boron nitride*, J. Phys. Chem. Solids **62**, 1331 (2001).

74. K. Watanabe, T. Taniguchi, and H. Kanda, *Direct-bandgap properties and evidence for ultraviolet lasing of hexagonal boron nitride single crystal*, Nat. Mater. **3**, 404 (2004).

75. K. P. Loh, I. Sakaguchi, M. N. Gamo, S. Tagawa, T. Sugino, and T. Ando, *Surface conditioning of chemical vapor deposited hexagonal boron nitride film for negative electron affinity*, Appl. Phys. Lett. **74**, 28 (1999).

76. A. Seidl, A. Görling, P. Vogl, J. A. Majewski, and M. Levy, *Generalized Kohn-Sham schemes and the band-gap problem*, Phys. Rev. B **53**, 3764 (1996).

77. L. Hedin, *New Method for Calculating the One-Particle Green's Function with Application to the Electron-Gas Problem*, Phys. Rev. **139**, A796 (1965).

78. X. Blase, A. Rubio, S. G. Louie, and M. L. Cohen, *Quasiparticle band structure of bulk hexagonal boron nitride and related systems*, Phys. Rev. B **51**, 6868 (1995).

79. A. Rubio, J. L. Corkill, and M. L. Cohen, *Theory of graphitic boron nitride nanotubes*, Phys. Rev. B **49**, 5081 (1994).

80. R. Arenal, A. C. Ferrari, S. Reich, L. Wirtz, J.-Y. Mevellec, S. Lefrant, A. Rubio, and A. Loiseau, *Raman Spectroscopy of Single-Wall Boron Nitride Nanotubes*, Nano Lett. **6**, 1812 (2006).

81. D. Golberg, P. M. F. J. Costa, O. Lourie, M. Mitome, X. Bai, K. Kurashima, C. Zhi, C. Tang, and Y. Bando, *Direct Force Measurements and Kinking under Elastic Deformation of Individual Multiwalled Boron Nitride Nanotubes*, Nano Lett. **7**, 2146 (2007).

82. E. Hernández, C. Goze, P. Bernier, and A. Rubio, *Elastic Properties of C and $B_xC_yN_z$ Composite Nanotubes*, Phys. Rev. Lett. **80**, 4502 (1998).

83. N. G. Chopra and A. Zettl, *Measurement of the elastic modulus of a multi-wall boron nitride nanotube*, Solid State Commun. **105**, 297 (1998).

84. M. M. J. Treacy, T. W. Ebbesen, and J. M. Gibson, *Exceptionally high Young's modulus observed for individual carbon nanotubes*, Nature **381**, 678 (1996).

85. X. Wei, M.-S. Wang, Y. Bando, and D. Golberg, *Tensile Tests on Individual Multi-Walled Boron Nitride Nanotubes*, Adv. Mater. **22**, 4895 (2010).

86. X. Blase, A. Rubio, S. G. Louie, and M. L. Cohen, *Stability and Band Gap Constancy of Boron Nitride Nanotubes*, Europhys. Lett. **28**, 335 (1994).

87. S. Azevedo, J. R. Kaschny, C. M. C. de Castilho, and F. de Brito Mota, *A theoretical investigation of defects in a boron nitride monolayer*, Nanotechnol. **18**, 495707 (2007).

88. S. Okada, *Atomic configurations and energetics of vacancies in hexagonal boron nitride: First-principles total-energy calculations*, Phys. Rev. B **80**, 161404 (2009).

89. V. M. Pereira, F. Guinea, J. M. B. Lopes dos Santos, N. M. R. Peres, and A. H. Castro Neto, *Disorder Induced Localized States in Graphene*, Phys. Rev. Lett. **96**, 036801 (2006).

90. V. M. Pereira, J. M. B. Lopes dos Santos, and A. H. Castro Neto, *Modeling disorder in graphene*, Phys. Rev. B **77**, 115109 (2008).

91. S. Wu, L. Jing, Q. Li, Q. W. Shi, J. Chen, H. Su, X. Wang, and J. Yang, *Average density of states in disordered graphene systems*, Phys. Rev. B **77**, 195411 (2008).

92. X. Liang, Z. Fu, and S. Y. Chou, *Graphene Transistors Fabricated via Transfer-Printing In Device Active-Areas on Large Wafer*, Nano Lett. **7**, 3840 (2007).

93. X. Li, X. Wang, L. Zhang, S. Lee, and H. Dai, *Chemically Derived, Ultrasmooth Graphene Nanoribbon Semiconductors*, Science **319**, 1229 (2008).

94. O. V. Yazyev and L. Helm, *Defect-induced magnetism in graphene*, Phys. Rev. B **75**, 125408 (2007).

95. O. V. Yazyev, *Magnetism in Disordered Graphene and Irradiated Graphite*, Phys. Rev. Lett. **101**, 037203 (2008).

96. Y.-W. Son, M. L. Cohen, and S. G. Louie, *Half-metallic graphene nanoribbons*, Nature **444**, 347 (2006).

97. P. Esquinazi, D. Spemann, R. Höhne, A. Setzer, K.-H. Han, and T. Butz, *Induced Magnetic Ordering by Proton Irradiation in Graphite*, Phys. Rev. Lett. **91**, 227201 (2003).

98. J. Barzola-Quiquia, P. Esquinazi, M. Rothermel, D. Spemann, T. Butz, and N. García, *Experimental evidence for two-dimensional magnetic order in proton bombarded graphite*, Phys. Rev. B **76**, 161403 (2007).

99. M. A. Ramos, J. Barzola-Quiquia, P. Esquinazi, A. Muñoz Martin, A. Climent-Font, and M. García-Hernández, *Magnetic properties of graphite irradiated with MeV ions*, Phys. Rev. B **81**, 214404 (2010).

100. A. Kumar, D. K. Avasthi, J. C. Pivin, A. Tripathi, and F. Singh, *Ferromagnetism induced by heavy-ion irradiation in fullerene films*, Phys. Rev. B **74**, 153409 (2006).

101. A. L. Friedman, H. Chun, Y. J. Jung, D. Heiman, E. R. Glaser, and L. Menon, *Possible room-temperature ferromagnetism in hydrogenated carbon nanotubes*, Phys. Rev. B **81**, 115461 (2010).

102. S. Talapatra, P. G. Ganesan, T. Kim, R. Vajtai, M. Huang, M. Shima, G. Ramanath, D. Srivastava, S. C. Deevi, and P. M. Ajayan, *Irradiation-Induced Magnetism in Carbon Nanostructures*, Phys. Rev. Lett. **95**, 097201 (2005).

103. Y. Wang, Y. Huang, Y. Song, X. Zhang, Y. Ma, J. Liang, and Y. Chen, *Room-Temperature Ferromagnetism of Graphene*, Nano Lett. **9**, 220 (2009).

104. M. Sepioni, R. R. Nair, S. Rablen, J. Narayanan, F. Tuna, R. Winpenny, A. K. Geim, and I. V. Grigorieva, *Limits on Intrinsic Magnetism in Graphene*, Phys. Rev. Lett. **105**, 207205 (2010).

105. R. Grantab, V. B. Shenoy, and R. S. Ruoff, *Anomalous strength characteristics of Tilt Grain Boundaries in Graphene*, (2010), arXiv:1007.4985v1.

106. F. Ding, K. Jiao, M. Wu, and B. I. Yakobson, *Pseudoclimb and Dislocation Dynamics in Superplastic Nanotubes*, Phys. Rev. Lett. **98**, 075503 (2007).

107. B. P. Uberuaga, S. J. Stuart, and A. F. Voter, *Parallel replica dynamics for driven systems: Derivation and application to strained nanotubes*, Phys. Rev. B **75**, 014301 (2007).

108. J. Y. Huang, S. Chen, Z. Q. Wang, K. Kempa, Y. M. Wang, S. H. Jo, G. Chen, M. S. Dresselhaus, and Z. F. Ren, *Superplastic carbon nanotubes*, Nature **439**, 281 (2006).

109. H. Stahl, J. Appenzeller, R. Martel, P. Avouris, and B. Lengeler, *Intertube Coupling in Ropes of Single-Wall Carbon Nanotubes*, Phys. Rev. Lett. **85**, 5186 (2000).

110. B. Biel, F. J. García-Vidal, A. Rubio, and F. Flores, *Anderson Localization in Carbon Nanotubes: Defect Density and Temperature Effects*, Phys. Rev. Lett. **95**, 266801 (2005).

111. L. Chico, M. P. López Sancho, and M. C. Muñoz, *Carbon-Nanotube-Based Quantum Dot*, Phys. Rev. Lett. **81**, 1278 (1998).

112. M. Bockrath, W. Liang, D. Bozovic, J. H. Hafner, C. M. Lieber, M. Tinkham, and H. Park, *Resonant Electron Scattering by Defects in Single-Walled Carbon Nanotubes*, Science **291**, 283 (2001).

113. Z. Ni, A. Ishaq, L. Yan, J. Gong, and D. Zhu, *Enhanced electron field emission of carbon nanotubes by Si ion beam irradiation*, J. Phys. D: Appl. Phys. **42**, 075408 (2009).

114. M. Sammalkorpi, A. Krasheninnikov, A. Kuronen, K. Nordlund, and K. Kaski, *Irradiation-induced stiffening of carbon nanotube bundles*, Nucl. Instrum. Methods Phys. Res., Sect. B **228**, 142 (2005), proceedings of the Seventh International Conference on Computer Simulation of Radiation Effects in Solids.

115. V. Skakalova, A. B. Kaiser, and S. Roth, *Raman mode shifts correlated with conductivity and Young's modulus changes in modified carbon nanotube networks*, Phys. Status Solidi RRL **2**, 62 (2008).

116. M. S. Si, J. Y. Li, H. G. Shi, X. N. Niu, and D. S. Xue, *Divacancies in graphitic boron nitride sheets*, Europhys. Lett. **86**, 46002 (2009).

117. M. Terrones, J.-C. Charlier, A. Gloter, E. Cruz-Silva, E. Terrés, Y. B. Li, A. Vinu, Z. Zanolli, J. M. Dominguez, H. Terrones, Y. Bando, and D. Golberg, *Experimental and Theoretical Studies Suggesting the Possibility of Metallic Boron Nitride Edges in Porous Nanourchins*, Nano Lett. **8**, 1026 (2008).

118. H. F. Bettinger, T. Dumitrică, G. E. Scuseria, and B. I. Yakobson, *Mechanically induced defects and strength of BN nanotubes*, Phys. Rev. B **65**, 041406 (2002).

119. P. Zhang and V. H. Crespi, *Plastic deformations of boron-nitride nanotubes: An unexpected weakness*, Phys. Rev. B **62**, 11050 (2000).

120. D. Golberg, Y. Bando, K. Kurashima, and T. Sato, *Synthesis and characterization of ropes made of BN multiwalled nanotubes*, Scr. Mater. **44**, 1561 (2001).

121. L. Tapasztó, G. Dobrik, P. Nemes-Incze, G. Vertesy, P. Lambin, and L. P. Biró, *Tuning the electronic structure of graphene by ion irradiation*, Phys. Rev. B **78**, 233407 (2008).

122. E. Ruska, *The early development of electron lenses and electron microscopy* (Hirzel, Stuttgart, 1980), translated by T. Mulvey.

123. D. J. Gardiner, *Practical Raman spectroscopy* (SPringer-Verlag, New York, 1989).

124. A. C. Ferrari and J. Robertson, *Interpretation of Raman spectra of disordered and amorphous carbon*, Phys. Rev. B **61**, 14095 (2000).

125. M. M. Lucchese, F. Stavale, E. H. M. Ferreira, C. Vilani, M. V. O. Moutinho, R. B. Capaz, C. A. Achete, and A. Jorio, *Quantifying ion-induced defects and Raman relaxation length in graphene*, Carbon **48**, 1592 (2010).

126. E. H. Martins Ferreira, M. V. O. Moutinho, F. Stavale, M. M. Lucchese, R. B. Capaz, C. A. Achete, and A. Jorio, *Evolution of the Raman spectra from single-, few-, and many-layer graphene with increasing disorder*, Phys. Rev. B **82**, 125429 (2010).

127. M. S. Dresselhaus, A. Jorio, M. Hofmann, G. Dresselhaus, and R. Saito, *Perspectives on Carbon Nanotubes and Graphene Raman Spectroscopy*, Nano Lett. **10**, 751 (2010).

128. F. Tuinstra and J. L. Koenig, *Raman Spectrum of Graphite*, J. Chem. Phys. **53**, 1126 (1970).

129. Y. Wang, D. C. Alsmeyer, and R. L. McCreery, *Raman spectroscopy of carbon materials: structural basis of observed spectra*, Chem. Mater. **2**, 557 (1990).

130. M. P. Allen and D. J. Tildesley, *Computer Simulation of Liquids* (Oxford University Press, Oxford, England, 1989).

131. M. Born and R. Oppenheimer, *Zur Quantentheorie der Molekeln*, Ann. Phys. **389**, 457 (1927).

132. B. J. Alder and T. E. Wainwright, *Phase Transition for a Hard Sphere System*, J. Chem. Phys. **27**, 1208 (1957).

133. B. J. Alder and T. E. Wainwright, *Studies in Molecular Dynamics. I. General Method*, J. Chem. Phys. **31**, 459 (1959).

134. B. J. Alder and T. E. Wainwright, *Studies in Molecular Dynamics. II. Behavior of a Small Number of Elastic Spheres*, J. Chem. Phys. **33**, 1439 (1960).

135. J. E. Lennard-Jones, *On the Determination of Molecular Fields. II. From the Equation of State of a Gas*, Proc. R. Soc. Lond. A **106**, 463 (1924).

136. P. M. Morse, *Diatomic Molecules According to the Wave Mechanics. II. Vibrational Levels*, Phys. Rev. **34**, 57 (1929).

137. J. F. Ziegler, J. P. Biersack, and M. D. Ziegler, *The Stopping and range of Ions in Matter* (SRIM Co., Chester, Maryland, 2008).

138. J. Tersoff, *New empirical approach for the structure and energy of covalent systems*, Phys. Rev. B **37**, 6991 (1988).

139. J. Tersoff, *Empirical Interatomic Potential for Carbon, with Applications to Amorphous Carbon*, Phys. Rev. Lett. **61**, 2879 (1988).

140. D. W. Brenner, O. A. Shenderova, J. A. Harrison, S. J. Stuart, B. Ni, and S. B. Sinnott, *A second-generation reactive empirical bond order (REBO) potential energy expression for hydrocarbons*, J. Phys. Condens. Matter **14**, 783 (2002).

141. K. Albe, *Computersimulationen zu Struktur und Wachstum von Bornitrid* (der Technischen Universität, Dresden, 1998), ph.D dissertation.

142. K. Albe and W. Möller, *Modelling of boron nitride: Atomic scale simulations on thin film growth*, Comput. Mater. Sci. **10**, 111 (1998).

143. K. Nordlund, 2010, PARCAS computer code. The main principles of the molecular dynamics algorithms are presented in [174, 175]. The adaptive time step and electronic stopping algorithms are the same as in [176].

144. H. J. C. Berendsen, J. P. M. Postma, W. F. van Gunsteren, A. DiNola, and J. R. Haak, *Molecular dynamics with coupling to external bath*, J. Chem. Phys. **81**, 3684 (1984).

145. D. Marx and J. Hutter, Ab Initio *Molecular Dynamics: Basic Theory and Advanced Methods* (Cambridge University Press, Cambridge, 2009).

146. P. Hohenberg and W. Kohn, *Inhomogeneous Electron Gas*, Phys. Rev. **136**, B864 (1964).

147. W. Kohn and L. J. Sham, *Self-Consistent Equations Including Exchange and Correlation Effects*, Phys. Rev. **140**, A1133 (1965).

148. Program TRIM (2008) by J.F. Ziegler and J.P. Biersack, http://www.srim.org.

149. G. H. Kinchin and R. S. Pease, *The displacement of Atoms in Solids by Radiation*, Rep. Prog. Phys. **18**, 1 (1955).

150. J. Lindhard, V. Nielsen, M. Scharff, and P. V. Thomsen, *Integral equations governing radiation effects. (Notes on atomic collisions, III)*, Kgl. Danske Videnskab., Selskab. Mat. Fys. Medd. **33**, (1963).

151. M. T. Robinson, *Nuclear Fission Reactors* (British Nuclear Energy Society, London, 1970).

152. K. A. Fichthorn and W. H. Weinberg, *Theoretical foundations of dynamical Monte Carlo simulations*, J. Chem. Phys. **95**, 1090 (1991).

153. A. Krasheninnikov, P. Lehtinen, A. Foster, and R. Nieminen, *Bending the rules: Contrasting vacancy energetics and migration in graphite and carbon nanotubes*, Chem. Phys. Lett. **418**, 132 (2006).

154. F. Banhart, *Irradiation effects in carbon nanostructures*, Rep. Prog. Phys. **62**, 1181 (1999).

155. Y. Gan, J. Kotakoski, A. V. Krasheninnikov, K. Nordlund, and F. Banhart, *The diffusion of carbon atoms inside carbon nanotubes*, New J. Phys. **10**, 023022 (2008).

156. J. Liu, R. Neumann, C. Trautmann, and C. Müller, *Tracks of swift heavy ions in graphite studied by scanning tunneling microscopy*, Phys. Rev. B **64**, 184115 (2001).

157. M. Caron, H. Rothard, M. Toulemonde, B. Gervais, and M. Beuve, *Theoretical and experimental study of electronic temperatures in heavy ion tracks from Auger electron spectra and thermal spike calculations*, Nucl. Instrum. Methods Phys. Res., Sect. B **245**, 36 (2006).

158. T. Kunert and R. Schmidt, *Excitation and Fragmentation Mechanisms in Ion-Fullerene Collisions*, Phys. Rev. Lett. **86**, 5258 (2001).

159. K. Eder, D. Semrad, P. Bauer, R. Golser, P. Maier-Komor, F. Aumayr, M. Peñalba, A. Arnau, J. M. Ugalde, and P. M. Echenique, *Absence of a "Threshold Effect" in the Energy Loss of Slow Protons Traversing Large-Band-Gap Insulators*, Phys. Rev. Lett. **79**, 4112 (1997).

160. A. Zobelli, C. P. Ewels, A. Gloter, and G. Seifert, *Vacancy migration in hexagonal boron nitride*, Phys. Rev. B **75**, 094104 (2007).

161. L. Sun, F. Banhart, A. V. Krasheninnikov, J. A. Rodríguez-Manzo, M. Terrones, and P. M. Ajayan, *Carbon Nanotubes as High-Pressure Cylinders and Nanoextruders*, Science **312**, 1199 (2006).

162. J. Kotakoski, A. V. Krasheninnikov, and K. Nordlund, *Energetics, structure, and long-range interaction of vacancy-type defects in carbon nanotubes: Atomistic simulations*, Phys. Rev. B **74**, 245420 (2006).

163. A. Misra, P. Tyagi, M. Singh, D. Misra, J. Ghatak, P. Satyam, and D. Avasthi, *Structural damage on multiwalled carbon nanotubes and encapsulated single crystal nickel nanorods irradiated with Au+7 ions of 100 MeV*, Diamond Relat. Mater. **15**, 300 (2006).

164. K. Heinig, T. Müller, B. Schmidt, M. Strobel, and W. Möller, *Interfaces under ion irradiation: growth and taming of nanostructures*, Appl. Phys. A **77**, 17 (2003).

165. M. Williams and E. Arakawa, *Optical properties of glassy carbon from 0 to 82 eV*, J. Appl. Phys. **43**, 3460 (1972).

166. A. Zobelli, A. Gloter, C. P. Ewels, G. Seifert, and C. Colliex, *Electron knock-on cross section of carbon and boron nitride nanotubes*, Phys. Rev. B **75**, 245402 (2007).

167. W. A. McKinley and H. Feshbach, *The Coulomb Scattering of Relativistic Electrons by Nuclei*, Phys. Rev. **74**, 1759 (1948).

168. K. Albe, Computersimulationen zu Struktur und Wachstum von Bornitrid, Ph.D dissertation, der Technischen Universität Dresden, 1998.

169. O. Lehtinen and J. Kotakoski, *Ion beam damage simulator for graphene*. 2010, http://www.helsinki.fi/nanocarbon/tools/ikmc. The set of simulated ion species (He, Ne, Ar, Kr, Xe and Ga) was chosen to give a good representation of a large range of ion masses plus Ga as a special case being a frequently used ion in FIB systems. The selection of ions in the code is being extended, however, and new ions and energies will be added once the calculations are completed.

170. J. Ullmann, J. E. E. Baglin, and A. J. Kellock, *Effects of MeV ion irradiation of thin cubic boron nitride films*, J. Appl. Phys. **83**, 2980 (1998).

171. S. Mansouri, P. Marie, C. Dufour, G. Nouet, I. Monnet, and H. Lebius, *Swift heavy ions effects in III-V nitrides*, Nucl. Instrum. Methods Phys. Res., Sect. B **266**, 2814 (2008).

172. J. N. Coleman *et al.*, *Two-Dimensional Nanosheets Produced by Liquid Exfoliation of Layered Materials*, Science **331**, 568 (2011).

173. K. S. Novoselov, D. Jiang, F. Schedin, T. J. Booth, V. V. Khotkevich, S. V. Morozov, and A. K. Geim, *Two-dimensional atomic crystals*, PNAS **102**, 10451 (2005).

174. K. Nordlund, M. Ghaly, R. S. Averback, M. Caturla, T. Diaz de la Rubia, and J. Tarus, *Defect production in collision cascades in elemental semiconductors and FCC metals*, Phys. Rev. B **57**, 7556 (1998).

175. M. Ghaly, K. Nordlund, and R. S. Averback, *Molecular dynamics investigations of surface damage produced by keV self-bombardment of solids*, Phil. Mag. A **79**, 795 (1999).

176. K. Nordlund, *Molecular dynamics simulation of ion ranges in the 1 – 100 keV energy range*, Comput. Mater. Sci. **3**, 448 (1995).